Universiteit Utrecht

Opleiding Natuur- en Sterrenkunde

Geant4 simulation of the calorimetric application of the ALPIDE CMOS sensor

Bachelor Thesis

Jerom Baas

Supervisors:

Dr. ing. N. van der Kolk
Subatomic Physics (SAP)

Prof. Dr. T. Peitzmann
Subatomic Physics (SAP)

January 16, 2019

Abstract

In this research the calorimetric application of the ALPIDE CMOS sensors has been studied through Geant4 Monte-Carlo simulations of a prototype for this sensor. Simulations for 4 and 24 layers of the prototype have been done for electrons of 50, 100, 150 and 180 GeV and simulations for one layer of the prototype with a tungsten absorber in front of it that is 0, 8, 20 and 28 mm thick. These results of tests for these prototypes can be compared to these simulations. The results show that these sensors are capable of measuring high energy particles and that the particle showers behave as expected. The results also show a lower secondary peak in the hits per event distribution for simulations of the 24 layer detector, which is likely caused by the small gap between the two ALPIDE chips used.

Contents

1 Introduction

In science we measure things to understand and develop our theories. William Thomson once wrote: "When you can measure what you are speaking about, and express it in numbers, you know something about it."[1] However, in modern science there is another tool to gain understanding about a matter. Rather than trying to measure something we can simulate it in a computer model. While the simulation is an extension of the theory, simulating something can give crucial insides in how the theory manifests itself.

In this research a Geant4 Monte-Carlo model of the new digital electromagnetic calorimeter (FoCal) prototype has been made. This electromagnetic calorimeter is designed to measure high energy particles in ALICE, one of the detector experiments at the Large Hadron Collider at CERN. The latest prototype is based on ALPIDE CMOS sensors. The simulations of this prototype make it possible to gain insights in the results this detector should produce when tested and makes it possible to compare the results of actual experiments to the simulated data.

The goal of this research is to implement a computer model that uses Geant4 Monte-Carlo simulations to produce simulated data for the new digital electromagnetic calorimeter (FoCal) prototype based on ALPIDE CMOS sensors.

In this thesis the prototype has been simulated for a few different cases. It has been simulated for 4 layers of the prototype and for 28 layers of the prototype. It has also been simulated for one layer of the prototype with a tungsten absorber in front of it that is 0, 8, 20 and 28 mm thick. All of these simulations have been done for electrons of 50, 100, 150 and 180 GeV. The results show that this prototype is able to measure high energy electrons, which create a shower inside the detector.

The remainder of this thesis is ordered as follows. In chapter 2 the theoretical background is discussed. In chapter 3 the method used for the simulations is discussed. The results for these simulations are presented in chapter 4. Chapter 5 is the conclusion for this research and chapter 6 contains a discussion of the research and the results.

2 Theoretical Background

2.1 ALICE

In this thesis a simulation of detector elements for a future detector to be used in ALICE has been performed. ALICE stands for 'A Large Ion Collider Experiment'. ALICE is one of the detector experiments at the Large Hadron Collider at CERN.[2] The ALICE detector was designed to study what happens to particles at extreme energy densities. These high energy densities are achieved by using the Large Hadron Collider to collide lead-ions. These ions are accelerated to an energy of 5.02 TeV for each colliding pair of nucleons.[3] During the collisions the nucleons smash into each other with such energy that it leads to very high temperatures of up to 100,000 times the temperature of the center of the sun.[4]

In the very early stages of the universe, just after the big bang, the universe is believed to have been in a similar state. These heavy ion collisions recreate the conditions of the early universe and allow us to study them. Under these conditions the quarks and gluons that make up the protons and neutrons will not be confined by the strong force anymore. Thus a quark gluon plasma forms.

Normally quarks are bound by the strong interaction and form protons and neutrons. The gluons are the mediator for this strong force. Most of the strong force is well understood, however there are still two unresolved questions: Why are quarks confined, and what is the mechanism of the creation of mass? Quarks have never been seen in isolation. They appear to be bound together inside larger particles such as protons and neutrons. This is what is known as confinement. The exact cause for this confinement is still unclear. When the quarks are bound together into larger particles, such as protons, the mass of the quarks doesn't seem to account for the mass of the particle. For example, the three quarks that make up protons and neutrons only account for one percent of their mass. It's unclear where the rest of the mass comes from.

When the temperatures get high enough that there is no confinement anymore, the quark gluon plasma forms. The existence of this quark gluon plasma and its properties are important issues in quantum chromodynamics, the theory that deals with the strong interaction between quarks and gluons.[5]

ALICE was designed to measure these heavy ion collisions which take place at its center. In addition, ALICE is measuring collisions of two protons and of protons with nuclei, where one can learn more about the fundamental interactions and the initial constituents of protons and nuclei. More specifically it measures the particles produced during these collisions. To properly measure these particles it observations with many different instruments in different positions are needed. ALICE measures how powerful the collision was, it tracks charged particles and identifies them. Particular care is taken to also measure photons, which cannot be seen directly in a tracking device. To catch these photons, amongst others an electromagnetic calorimeter is used which can measure them over a wide area and also catch groups of closeby particles called jets.[6]

2.2 The FoCal proposal

The ALICE Collaboration is planning to upgrade its experimental apparatus. To reach their physics goals they presented plans to upgrade the current detector by enhancing its low-momentum vertexing and tracking capabilities and to make it possible to take data at higher rates, which should enable precision studies of lead ion collisions.[7]

For this upgrade an electromagnetic calorimeter based on SiW technology is being developed. One of the main design challenges is the requirement to discriminate decay photons from direct photons at high energy. This requires an excellent position resolution which can be achieved with a highly granular readout. The design being considered consists of layers with silicon detectors as active devices and tungsten plates as absorbers. The silicon sensors being considered are monolithic active pixel sensors with a binary readout. These sensors have pixels with a size of about 30x30 µm which allows for high granularity.[8]

2.3 Calorimetry

This section will mostly follow Calorimetry for Particle physics by C W Fabjan and F Gianotti [9] and the section about particle detectors by C Grupen and B Shwartz.[10]

Calorimetry is the usage of a calorimeter to detect particles. The calorimeter absorbs the particle's energy and transforms it into a measurable quantity. Photons, electrons and hadrons interact with the detector's material through electromagnetic or strong processes which results in a shower of secondary particles if the particle's energy is high enough ($\geq$ 1 GeV). This shower is a cascade of secondary particles with progressively degraded energy. The showering allows the initial particle to deposit its energy much more efficiently as the energy will be distributed over multiple particles that interact with the material rather than just one particle that interacts with the material.

There are two broad types of calorimeters. Electromagnetic calorimeters mainly measure electrons and photons, which shower due to their electromagnetic interaction with the detector's material. Hadronic calorimeters can measure hadrons, which shower due to their strong and electromagnetic interactions with the material.

Furthermore, there are two different ways to construct a calorimeter. It can be constructed as sampling calorimeters or homogeneous calorimeters. Sampling calorimeters are made out of alternating layers: An absorber, a dense material that creates a particle shower, and a material that can be used to turn the deposited energy into a signal. On the other hand, homogenous calorimeters are made up of a single material that performs both the task of absorbing the particle and the task of converting the deposited energy into a measurable signal. Sampling calorimeters allow the usage of an optimal absorber which produces a shower that quickly evolves, however only a small part of the particles energy is deposited in a sensitive area of the detector that turns it into output. Homogeneous calorimeters have a much better energy resolution because all of the particle's energy is absorbed in the sensitive area of the detector. These calorimeters are less suitable for position measurements and parti-

cle identification because they cannot easily be segmented and they require a material that can adequately perform the task of the absorber and as well as measure the deposited energy.

Calorimeters are very suitable detectors for high energy physics for several reasons. First of all, the calorimeter energy resolution improves with energy as $1/\sqrt{E}$, which makes their resolution for high energy particles relatively good. They are also capable of detecting both charged particles as well as neutral hadrons. Furthermore, by analyzing the shower it is possible to determine the position and direction of the particle and identify different particles. Lastly, the shower length increases logarithmically with energy, which thus means that the detector thickness also only needs to increase logarithmically. Because of this calorimeters require little space. Especially the fact that calorimeters can also measure particles that aren't charged makes calorimeters very useful detectors for ALICE. The main downside of a calorimeter is that it destroys the particle in the process of measuring it.

2.4 Electromagnetic Showers

Because the calorimeter that has been simulated in this research is an electromagnetic calorimeter, it is of special interest to study the physics behind the electromagnetic showers. The interaction of photons and electrons with matter is well understood. For energies above about 10 MeV the main way electrons lose energy is through bremsstrahlung. Photons mainly lose energy by pair production of an electron and positron pair. When the energy exceeds 1 GeV these processes are roughly independent of the energy. At energies of over 100 MeV the electrons and photons lose their energy almost exclusively by bremsstrahlung and pair production respectively. At lower energy levels, electrons lose their energy primarily through ionizing the particles of the material and thermal excitations. Photons lose their energy through Compton scattering and the photoelectric effect.

When high energy charged particles are decelerated by the Coulomb field of the nucleus of an atom, a part of their energy will be emitted in the form of a photon. This is known as bremsstrahlung. Particles with sufficiently high energy will thus create secondary photons through bremsstrahlung. If these photons have enough energy (at least 1.022 MeV) they will produce an electron-positron pair when interacting with a nucleus, thus creating even more electrons and positrons (pair production). The secondary particles generated from high energy photons and electrons will thus generate even more secondary particles until the energy of the secondary particles is below a certain threshold for which bremsstrahlung and pair production will not occur anymore. This leads to a cascade of particles with decreasing energies.

When the energies of the particles get lower, they mainly dissipate their energy by ionization, excitation, Compton scattering and the photoelectric effect. By exciting atoms electrons are turned into low energy photons. Together with ionization the lower energy electrons lose their energy without producing secondary particles. At lower energy the photons start losing their energy through Compton scattering and the photoelectric effect. In Compton scattering photons scatter of nearly free electrons and is absorbed. A photon with a lower energy is then emitted. The photoelectric effect is the complete absorption of photons by atoms. Again no

secondary particles are produced in these processes. This means that particles will produce a shower as long as their energy is sufficient for Bremsstrahlung and pair production. When the energy of the secondary particles becomes lower, the ionization, excitation, Compton effect and photoelectric effect will become more dominant and thus the amount of showering reduces until the secondary particles stop generating even more particles. At that point the number of particles in the shower stops increasing and all the remaining energy is dissipated without generating new particles.

The characteristics of the particle shower can be described with the use of the radiation length X_0, which depends on the properties of the material:

$$X_0(\mathrm{g/cm^2}) \approx \frac{716 \text{ g cm}^{-2} A}{Z(Z+1)\ln(287/\sqrt{Z})} \ . \tag{1}$$

The radiation loss of an electron is described by the following simplified formula:

$$-\left(\frac{dE}{dx}\right)_{\mathrm{rad}} = \frac{E}{X_0} \ . \tag{2}$$

This differential equation can be solved, which results in the following:

$$\langle E(x) \rangle = E_0 \ e^{-\frac{x}{X_0}} \ . \tag{3}$$

This means that the energy of an electron will be reduced by $1/e$ of its initial energy after it has travelled a length x equal to the radiation length. The radiation length thus is a measure for the rate at which electrons lose energy by bremsstrahlung.

The energy losses of photons can be described in a similar fashion. For high energy photons the energy of the photon is mainly absorbed through pair production. For an incoming beam with initial intensity I_0, the intensity after the photons have travelled a certain distance x is given by

$$\langle I(x) \rangle = I_0 \ e^{-\frac{7}{9}\frac{x}{X_0}} \ . \tag{4}$$

In this case the intensity will be reduced by $1/e$ of the initial intensity after the photons have travelled a length of $9X_0/7$. This means that the energy loss per distance travelled is described by the radiation length for both the electrons and photons. Thus the radiation length is a measure for the shower length of incoming particles.

It is convenient to consider the shower length in terms of the distance travelled normalized in radiation lengths as

$$t = \frac{x}{X_0} \ . \tag{5}$$

The development of the an electromagnetic shower can be simplified into the following model: Assume that an incoming photon of energy E_0 takes one radiation length to produce a positron-electron pair, which in turn produce a photon each through Bremsstrahlung after

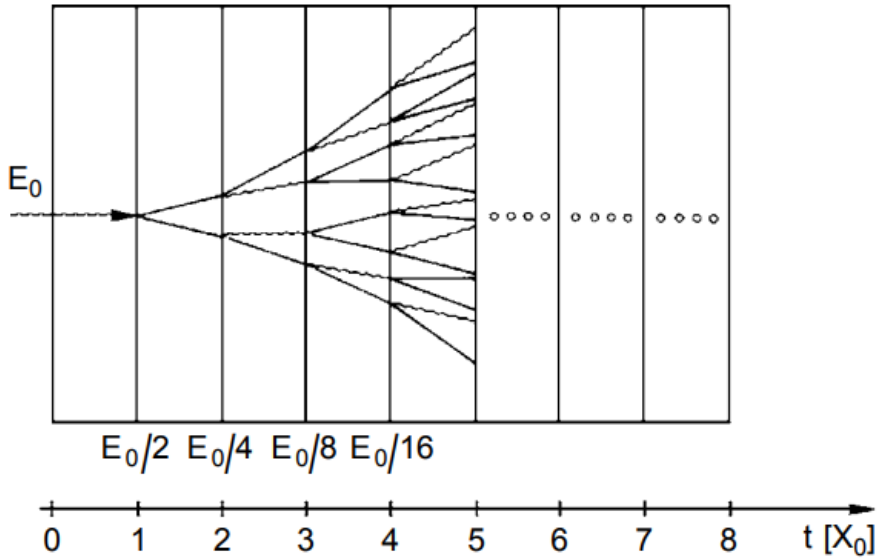

Figure 1: A simplified model for the shower of high energy electrons and photons.[10]

one radiation length. Furthermore assume that the energy of the particles is split evenly between them. This model is visualized in figure 1 and showcases how high energy electrons and photons create a particle shower in a material through bremsstrahlung and pair production.

This also visualizes how the radiation length is related to the longitudinal profile of the particle shower. The lower the radiation length, the shorter the particle shower will be. This means that materials with a lower radiation length make for excellent absorbers.

In this model the number of particles in the shower doubles each time the particles travel a distance of t. This means that the number of particles in the shower is given by

$$N(t) = 2^{\,t} \ , \tag{6}$$

where t is given by equation 5. The energy will be split between all the individual particles and thus the energy per particle at distance t is equal to $E_0/N(t)$. This can be rewritten as

$$E(t) = E_0 \cdot 2^{-t} \ . \tag{7}$$

Now assume that the multiplication of the shower particles continue as long as the energy per particle is above a certain threshold. When the energy falls below that threshold processes like ionization or Compton scattering, which do not produce secondary particles, start to dominate. Thus we can write the critical energy as

$$E_c = E_0 \cdot 2^{-t_{max}} \ , \tag{8}$$

where t_{max} represents the maximum amount of radiation lengths that the particles can travel until the energy drops below the critical energy and the showering stops. This leads to

$$t_{max} = \frac{\ln(E_0/E_c)}{ln2} \propto \ln(E_0/E_c) \tag{9}$$

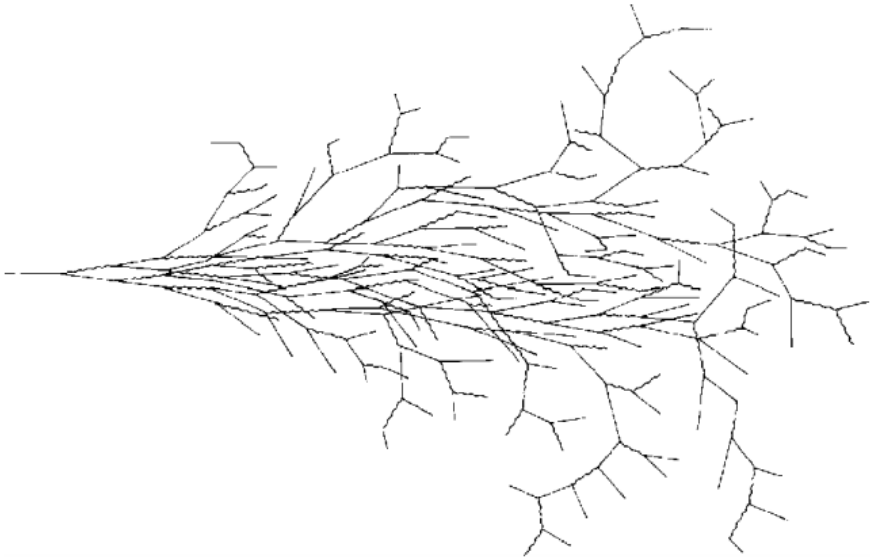

Figure 2: A schematic representation of an electromagnetic particle shower. The wavy lines represent photons while the solid lines represent electrons or positrons.[10]

In other words, the distance the particles need to travel scales logarithmically with the initial energy. This makes calorimeters excellent for particles with very high energies, as the calorimeter only need to scale in size logarithmically when the energy increases and thus can be made very compact.

In reality the shower development is much more complicated. The particles will not take exactly one radiation length to interact with the material through bremsstrahlung and pair production, but will do so randomly depending on their position relative to the material's atoms. The direction of the secondary particles will not be as simple either nor will the energy be split equally between the particles. The assumption that the shower stops when a particular energy is reached isn't quite accurate either. In reality the particles will start to lose energy through processes that do not produce secondary particles more and more, until eventually those processes start to dominate. While attempts have been made to describe the particle showers analytically, nowadays an accurate description can be obtained using Monte Carlo simulations. A more realistic particle shower can be seen in figure 2. The showers do however behave generally the same as in the simplified model.

The critical energy is a measure for the energy at which the particles start to shower less. It is defined in two ways. The first definition of the critical energy is the energy for which an electron loses as much energy through ionization as it does through Bremsstrahlung. The value of this energy depends on the material and is approximately equal to

$$\epsilon = \frac{610(710)\text{MeV}}{Z + 1.24(0.92)} \ . \tag{10}$$

The second definition for the critical energy is the energy at which the ionization loss per X_0 equals the electron energy E:

$$\frac{dE}{dx}(\text{ionization}) = \frac{E}{X_0} \ . \tag{11}$$

The exact expression for the position of the maximum of the shower, which is calculated in the simplified model in equation 9, is given by:

$$t_{max} \approx \ln \frac{E_0}{\epsilon} + t_0 \ , \tag{12}$$

where t_{max} is the amount of radiation lengths the maximum of the shower is at and t_0 is -0.5 for electrons and +0.5 for photons. Again we find that the position of the shower maximum depends logarithmically on the energy of the incident particle. Of course this means that the length required to contain most of the shower is actually longer than this. The length for which 95% of the shower is contained is approximated by

$$t_{95\%} \approx t_{max} + 0.08Z + 9.6 \ . \tag{13}$$

For a calorimeter that is about 25 radiation lengths thick most of the shower is contained.

The shower generally develops not only in longitudinal direction but also spreads out in transverse directions. This happens primarily due to scattering of the electrons and positrons away from the shower direction. Bremsstrahlung photons can also be emitted away from the shower actions and thus contribute towards the spread. The transverse size, integrated over the full shower depth, is given by the Molière radius. The Molière radius can be approximated as

$$R_M(\text{g/cm}^2) \approx 21\text{MeV}\frac{X_0}{\epsilon(\text{MeV})} \ . \tag{14}$$

Here the definition for the critical energy in equation 11 should be used. On average about 90% of the energy of the incoming particle is contained within a radius of 1 R_M. This means that the calorimeter should have a radius that is at least similar to that of the Molière radius, but preferably of multiple Molière radiuses to contain as much of the shower as possible.

Some of the energy of the particle will ultimately be lost. Due to possible constraints in cost the detector might have some longitudinal leakage particles because it would be cost and space inefficient to make the detector long enough to absorb all energy in the longitudinal direction. There will also be some lateral leakage. A fraction of the particles might scatter at such angles that they will leave the detector before having fully deposited their energy. Similarly particles might even scatter at angles so large that they will travel backwards and leave the detector before their energy has been fully absorbed. In practice detectors will also have inactive regions that are unable to detect particles. All of these factors reduce the energy resolution.

2.5 Prototype design

The prototype calorimeter that has been simulated in this research is a sampling calorimeter. It has layers that consist of a sensitive area of silicon and an absorber.

Material	Density (g/cm³)	X_0 (cm)	R_M (cm)
Cu	8.96	1.436	1.568
Pb	11.35	0.5612	1.602
W	19.30	0.3504	0.9327
Re	21.02	0.3183	0.8594
Pt	21.45	0.3051	0.8527

Figure 3: A table of different materials, their density, radiation length and Molière radius.[11]

In this case the chosen material for the absorber is tungsten. Tungsten has a rather small radiation length and Molière radius and thus is an excellent absorber. A sampling calorimeter is not restricted in its choice of absorber, as it does not need to perform the task of actually detecting the particles. Thus one of the main advantages is that it is possible to choose a great absorber like Tungsten. In figure 3 different radiation lengths and Molière radiuses for copper, lead, platinum and rhenium are shown as well as those for tungsten. This indicates that tungsten is an excellent choice. While there are some materials with an even lower radiation length and Molière radius, such as platinum and rhenium, tungsten is relatively cost efficient compared to those materials. Because of the small radiation length and Molière radius of tungsten it is possible to build a very compact detector. To contain most of the shower, the detector should be at least one Molière radius wide but preferably even wider to contain the majority of the shower. The thickness can be calculated using equation 13. For particles of the order of 100 MeV we find that $t_{95\%} \approx 18.2 \pm 0.5$ radiation lengths depending on if the incident particle is a photon or electron. For particles of 1 TeV this increases to approximately 20.5 ± 0.5 radiation lengths. So this means that the tungsten absorber layers should have a combined thickness of at least 21 radiation lengths to be able to absorb 95% of the energy of particles of 1 TeV and absorb most of the energy of particles in the 100 MeV energy range.

The sensitive area is made of silicon chips. These chips are ALPIDE chips with a pixel matrix of 1024x512 pixels. For each layer two chips are placed next to each other for a combined grid of 1024x1024 pixels. These chips are able to convert deposited energy into a binary signal in each pixel of either on or off. These silicon sensors will make the device a digital calorimeter. In this, the total number of pixels with a signal (called "hits") will be used to measure the energy of the incoming particle.

The tungsten absorber used in the prototype is 3 mm thick, and has x and y dimensions of 40 and 35 mm respectively. Two tungsten spacers are placed on each side to make sure the next layer doesn't rest directly on top of the chips. These are 0.5 mm thick and have x and y dimensions of 4 and 35 mm respectively. Each layer of tungsten is almost one radiation length thick. To properly absorb the showers of particles with energies of up to 1 TeV the detector needs to have slightly more than 21 layers. The radius of the detector is much larger than one Molière radius. This is necessary however, because particles will not always hit the detector at a 90 degree angle right at the middle, but might hit the detector away from the

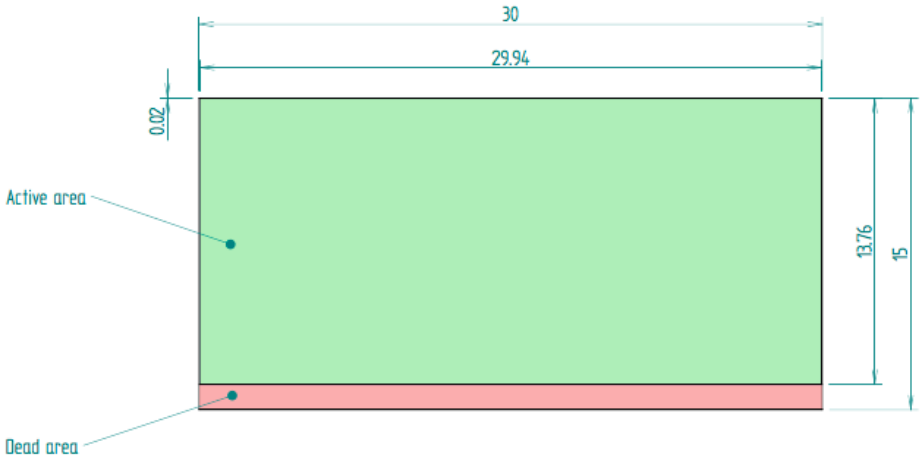

Figure 4: A schematic representation of the ALPIDE chips.

middle or at a relatively large angle. The width of this prototype should ensure that the majority of the energy of those particles will also be absorbed.

Each chip is 100 µm thick and has x and y dimensions of 30x15 mm. However, only the top 25 µm of the chip is actually sensitive, while the bottom 75 µm is an inactive area. Furthermore the last 1.24 mm in the y direction is inactive because that part is used to read out the chip. The chip has pixels with x and y dimensions of 29.24x26.88 µm. This means that, when you place all pixels next to each other, there is a 0.03 mm area in the x direction on both sides that is inactive. The active area of a chip is thus 25 µm thick and 29.94x13.76 mm in the x and y dimension. A schematic picture of the chips can be seen in figure 4. The two chips are then placed next to each other to form a 30x30 mm square. However, in practice it is not possible to place the chips exactly adjacent to each other. There actually is a 1 mm gap between the two chips. Lastly, the chips are attached to the absorber with a 20 µm layer of glue. The glue used is Araldite 2011. These chips are placed in between the spacers.

To actually read out these chips a layer of cables is placed onto the chips and these are connected to what is called a flex cable, or in short 'flex'. This flex carries the produced signal from the detector to the readout. The chip cables as well as the flex cables and boards are made of aluminium-polyimide dielectrics. The cables on top of the chip form a layer of 20 µm polyimide and 30 µm aluminium. The flex has four layers: a bottom layer of once again 20 µm polyimide and 30 µm aluminium, a spacer layer of 40 µm Kapton, then another identical layer of polyimide and aluminium and finally a cover layer of Kapton which is again 40 µm thick. This flex has x and y dimensions of 30x55 mm and is also placed in between the spacers. The chipcables are attached to the chips with a layer of 5 µm glue. The first layer of the flex is then attached with 8 µm glue. Between the first layer and the spacer is 3 µm of glue. Then the second layer is attached to the spacer with about 5 µm of glue. Then lastly the top cover layer is attached to the second layer with 3 µm of glue. The glue used

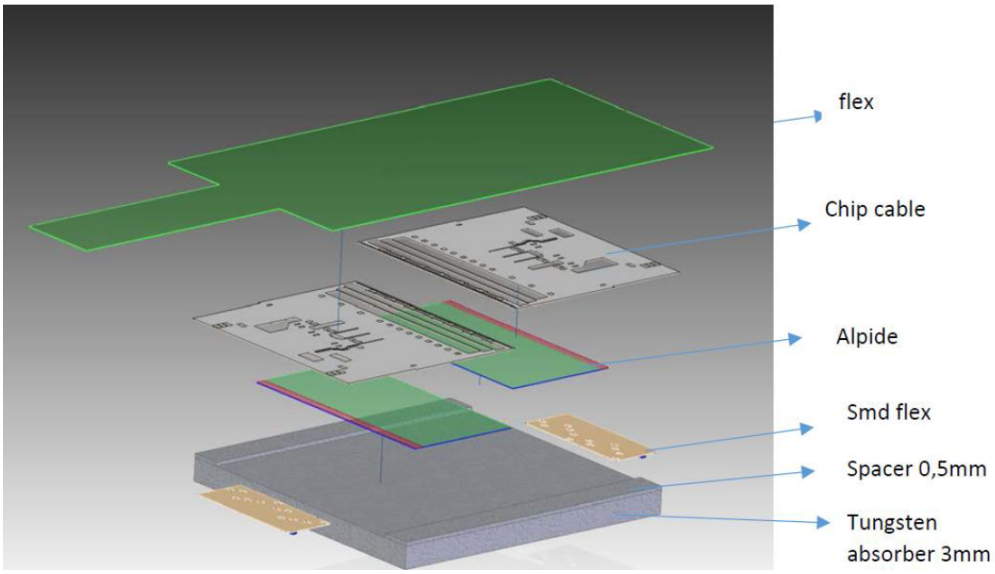

Figure 5: A schematic representation of one layer and its components.[12]

for this is also Araldite 2011.

Each layer will thus be 3.5 mm thick, and will have dimensions of 40x55 mm. A schematic picture of the layers can be seen in figure 5. Ultimately the detector should consist out of 24 of these layers stacked on top of each other. Given the calculations for the required amount of layers to absorb most of the particle shower, 24 layers seem to be adequate to absorb particles with extremely high energies.

2.6 Geant4

Geant4 is an object oriented toolkit based on C++ made to simulate particles that pass through matter. The simulations are done by specifying the detector's geometry, the physics processes to be used and the generation of initial particles. It simulates the interactions of particles using the Monte Carlo method. Most of this section will be following Geant4's physics reference manual.[13]

The Monte Carlo method is a numerical method that can be used to simulate processes. It is based on using random sampling to obtain numerical results. This method assumes that a system can be described by probability density functions. By then generating random samples according to this probability density function is can then use these samples to solve the processes of that system numerically. For the processes relevant for the particle showers generated inside a calorimeter it is hard to formulate the analytical equations and then numerically solve these. The Monte Carlo method makes it possible to obtain appropriate results without actually writing down and solving such complex equations, but instead solve them using a lot of random samples. The Monte Carlo method is especially useful for solving processes that are already stochastic of nature. In those cases the Monte Carlo steps actually correspond to steps in the simulated process. The Monte Carlo method is thus

excellent at describing the stochastic and complex interactions of particles with matter. In specific Geant4 uses a combination of composition and rejection Monte Carlo methods.[14][15]

The first task Geant4 needs to perform is the particle transport. In Geant4 the particle transport is simulated step by step. The step length from interaction to interaction is randomly sampled based on the mean free path of the interaction. This mean free path is calculated based on the cross section of a particular physics process and the density of the atoms in the material. The number density of the atoms of an element is given by

$$n = \frac{N\rho w}{A} \ , \tag{15}$$

where N is Avogadro's number, ρ the density of the medium, w the proportion of mass of this element and A the mass of a mole of this element. The mean free path of a certain process can then be calculated as

$$\lambda(E) = \left(\sum_i [n_i \cdot \sigma(Z_i, E)] \right)^{-1} \ , \tag{16}$$

where $\sigma(Z, E)$ is the cross section of the process per atom and the sum runs over all different elements that make up the medium. Geant4 thus models the mean free path as the probability of a particle with a certain cross section to collide with an atom. The average distance a certain particle travels without a certain process happening is thus equivalent to the average distance that a projectile with a cross section equal to the cross section of that process travels without colliding with an atom in the medium.

This mean free path can then be used to determine the distance the particle actually travels in the simulation. The mean free path can't be used to directly sample the probability of an interaction. For this, first define the number of mean free paths that a particle travels before interacting:

$$n_\lambda = \int_{x_1}^{x_2} \frac{dx}{\lambda(x)} \ . \tag{17}$$

Now if n_τ is a random variable that represents the number of mean free paths that the particle from a given point to the point of interaction, the probability distribution is given by

$$P(n_\tau < n_\lambda) = 1 - e^{-n_\lambda} \ . \tag{18}$$

The total number of free paths can then be sampled as $n_\lambda = -\log(\eta)$ with η a number from 0 to 1. After a step of length Δx completes, n_λ of this process is updated to

$$n'_\lambda = n_\lambda - \frac{dx}{\lambda(x)} \ . \tag{19}$$

If this process has the shortest value for n_λ this process triggers. So Geant4 determines the process for which n_λ has been sampled to be the shortest and then triggers that process in the next step, after which it updates n_λ for the other processes and chooses the next process to execute in the next step.

To make sure the particles are simulated when they enter a new material, the transportation process is used. This process determines the geometrical limits and calculates the length of a step that means the particle will cross into another volume. When that boundary is reached the transportation process locates the next volume that the particle will enter. It is also responsible for calculating the motion of a charged particle in an electromagnetic field. The equations of motions for this are solved with Runge Kutta methods.

Most of the physics processes are treated based on cross sections, similar to the particle transport. The hadronic physics can be simulated using different models, like the Fritiof model or the Bertini cascade model. Geant4 offers a number of premade physics lists which combine certain available models in different energy ranges. The available hadronic models are: The quark gluon string model (QGS), the Fritiof model (FTF), the Binary intra-nuclear cascade (BIC), the Bertini-style intra-nuclear cascade (BERT), the high precision neutron transport models (HP) and the precompound model for nuclear de-excitation. Standard electromagnetic physics describe the electromagnetic processes accurately, but there are some possible options. The EMV option contains faster but older electromagnetic processes. EMY and EMZ are more suitable for low energy electromagnetic processes. It is also possible to use the Livermore or Penelope based electromagnetic models.[16][17]

For the simulations in this thesis the FTFP_BERT physics list was used. This model uses the Fritiof model and the precompoud model for the hadronic physics and the standard electromagnetic options of Geant4. It is one of the recommended physics lists for high energy calorimetry. The other recommended physics list is QGSP_BERT, which uses the quark gluon string model for energies larger than 20 GeV. [18]

3 Methodology

3.1 Geometry

A Geant4 model has been made of the prototype detector. To do this some approximations have been made. The geometry of the flex that is placed on top of the detector chip has been simplified as a summary of three layers of the different compounds (glue, aluminium and polyimide) of the summed thickness of each of these materials in the flex. The complex structure of the different electric components was also completely ignored.

3.2 Particle Source

To generate particles, Geant4's General Particle Source has been used. This source was placed along the z-axis 17 meters from the detector and shoots particles along the z-axis with a Gaussian spread in the angle between the particles direction and the z-axis. The particles fired will have a 0.1 degree standard deviation in both the x- and y-direction. This means the particles will reach the detector within about a 3 millimeter radius from the origin. Unfortunately there is no precise data on the spread of the beam so this is only a rough estimate. The particle source has also been set to have a Gaussian spread in the energy profile of the particles with a standard deviation of one percent of the energy. Once again there is no precise data on the spread of the energy so this is only a rough estimate.

3.3 Output and data analysis

The Geant4 simulation gives a ROOT Tree file as output, which contains the position, energy deposited and the corresponding event for each step in the simulation. This data file was then analyzed using a ROOT script, which converted the position to the corresponding pixel and layer and then accumulated the deposited energy for each pixel. In reality the pixels of the detector can only be on or off, and thus the deposited energy will be translated to the pixel being either on or off. This thus has also been taken into account in the data analysis. The results will contain both the amount of deposited energy as well as the purely digital output which the detector will give. The former will allow for more insight in what is going on within the detector, while the latter can be used to compare the results from the simulation with results from experiments.

3.4 Simulations

A couple of different setups have been simulated in Geant4. There have been experiments with just one layer of the detector with a block of tungsten in front of it of differing thickness. This has been tested with no tungsten in front and with 8, 20 and 28 millimeters of tungsten in front of the detector. This means the detector will measure a different point of the particle shower depending on how thick the block of tungsten in front was. This was done for electrons with an energy of 50, 100, 150 and 180 GeV. These setups have been simulated in Geant4.

Currently four layers of the detector are done and will be tested. Simulations for a detector of four layers have been done for electrons with an energy of 50, 100, 150 and 180 GeV. The results from these simulations can be compared to the future experiments.

Because the detector will ultimately consist of 24 layers, a 24 layer detector has been simulated for electrons with an energy of 50, 100, 150 and 180 GeV. Once the construction of the detector has been finished, these simulations can be compared to future experiments.

Lastly, the four layer setup has also been simulated for cosmic muons with an energy of 5 GeV. Cosmic muons are an easy way to test the detector without having to place it in a particle accelerator. By simulating these muons it will be possible to compare experimental data from cosmic muons to the simulations.

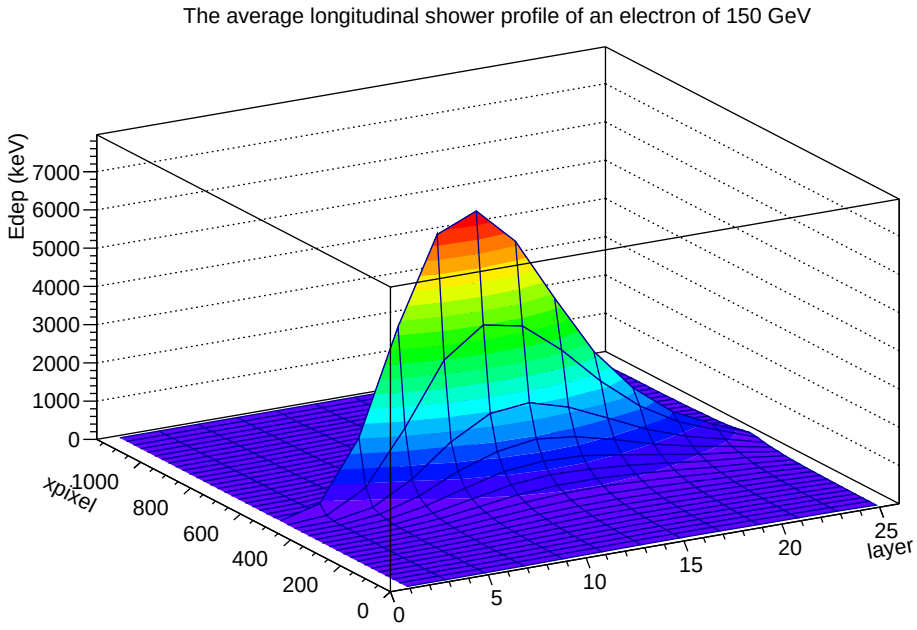

Figure 6: Average deposited energy per pixel as a function of pixel number in the x-direction and layer number.

4 Results

To keep this section compact, only the results for the 150 GeV simulations will be shown. The results for the other simulations will be shown in the appendix.

4.1 Benchmark

To have a benchmark to compare the other simulations to, the 24 layer setup has been simulated without the spread of the beam and without the gap between the two chips. The longitudinal shower profile for this simulation can be seen in figure 6 as the average deposited energy per pixel as a function of pixel number in the x-direction and layer number. The shower seems to be about 24 layers long, which corresponds to the theoretic value for $t_{95\%}$ for this detector. Because the particle enters the detector at exactly the same spot for each event, the peak of the shower profile is very sharp and high.

The average hits per event per pixel area integrated over all layers as a function of the pixel number in x- and y-direction that these particle showers give can be seen in figure 7. In this figure the 24 layers are stacked on top of each other in one single plot. This plot shows the average amount of times that a pixel is active in the simulated 1000 events. Since the pixel enters the detector at the exact same spot every time, that specific pixel and the pixels very close to it are on average active in multiple layers of the detector. The surrounding pixels are generally expected to be active in one to two layers. The further away from the

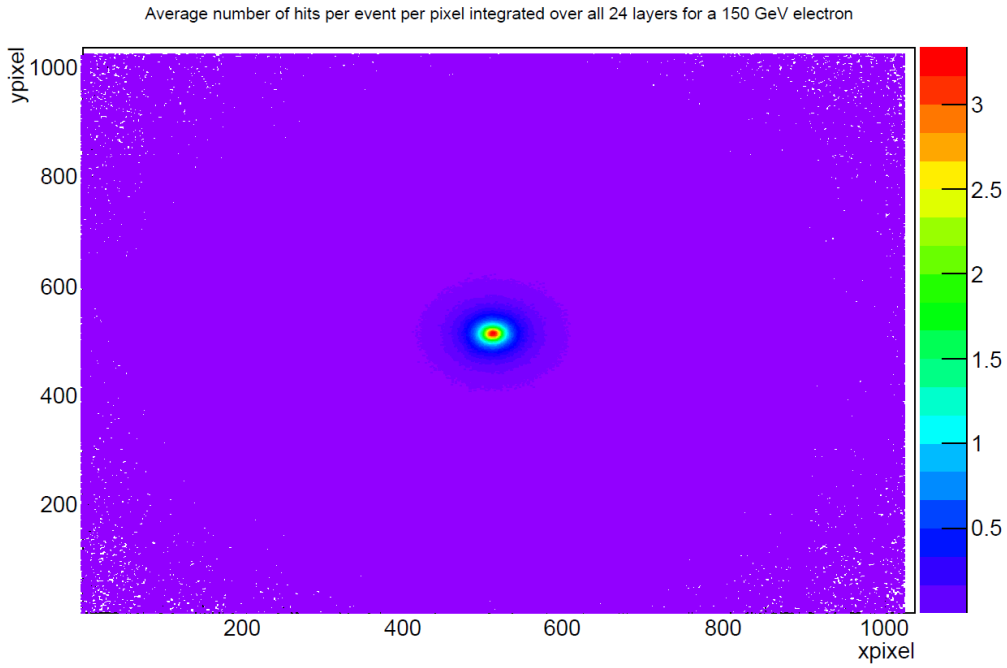

Figure 7: Average hits per event per pixel area integrated over all layers as a function of the pixel number in x- and y-direction for 24 layers.

center where the particle hit the detector the smaller the chance that a pixel is active. The pixels far away from the center of the detector are only rarely active.

It is also interesting to look at the spread of the particle beam used. This has been plotted in figure 8 as the average number of hits per event and per pixel area as a function of pixel number in x- and y- direction for a detector of one layer. This shows a simple Gaussian spread in the profile of the beam. For this simulation 10000 events have been used and the result has been averaged again. The density of hits in the middle is much higher than the density far away from this center, as is to be expected.

In figure 9 the number of hits per event is shown for a 150 GeV electron. This results in a clear peak at around 10000 hits.

4.2 24 layers

The average hits per event per pixel area integrated over all layers as a function of the x and y position is shown in figure 10 for a 24 layer detector with a spread in the particle source and a gap between the two chips. The gap between the two chips is clearly visible. The center of the detector is on average more active than the edges of the detector. In the benchmark it can be seen that generally much of the shower's energy is deposited close to the position where the particle enters. The spread of the beam will then smear out the activity of the pixels, with the center being the most active and the edges the least active. There are some clusters of increased activities far away from the center. These correspond to particles that

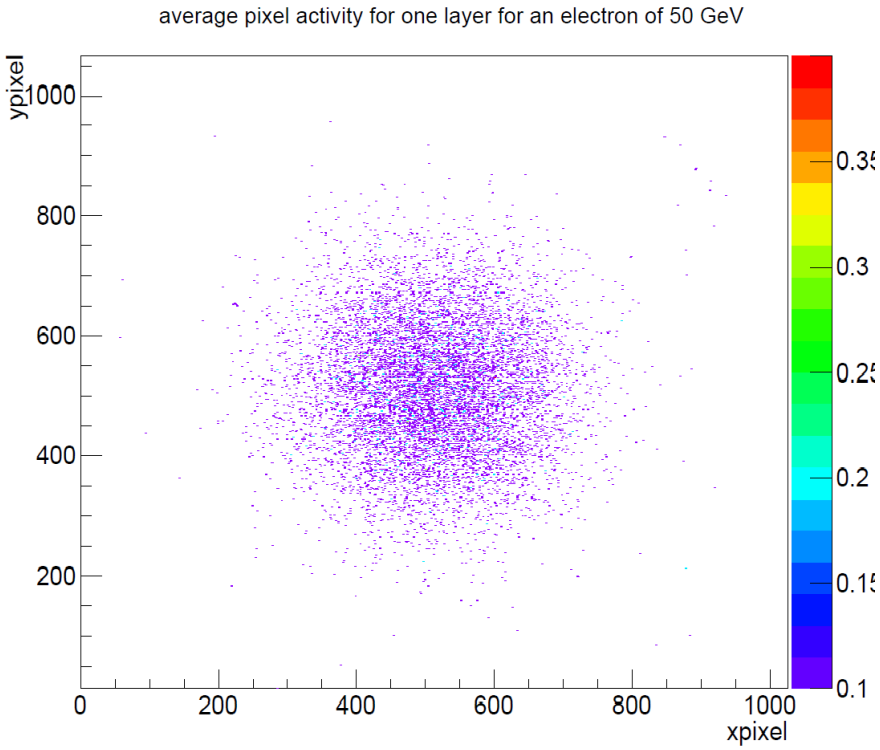

Figure 8: Average number of hits per event and per pixel area for the first layer layers as a function of pixel number in x- and y-direction.

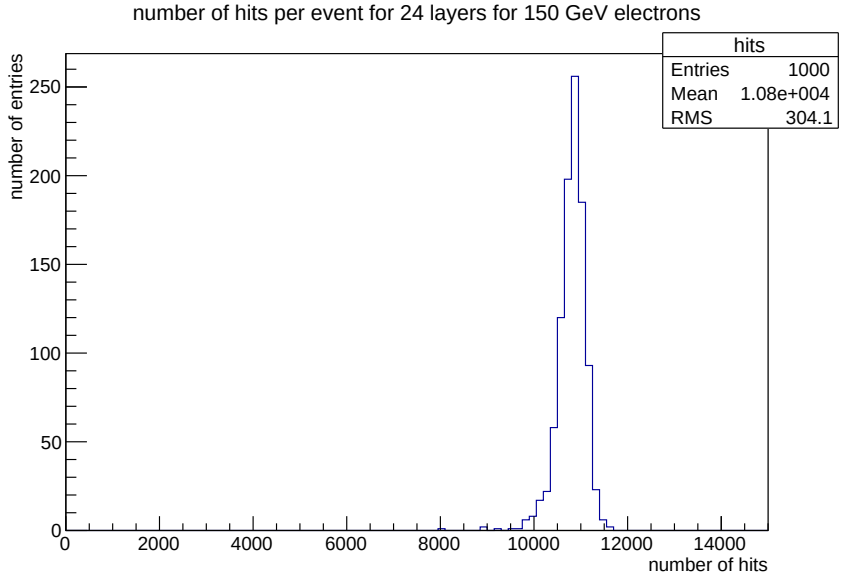

Figure 9: The number of hits per event for a 150 GeV electron

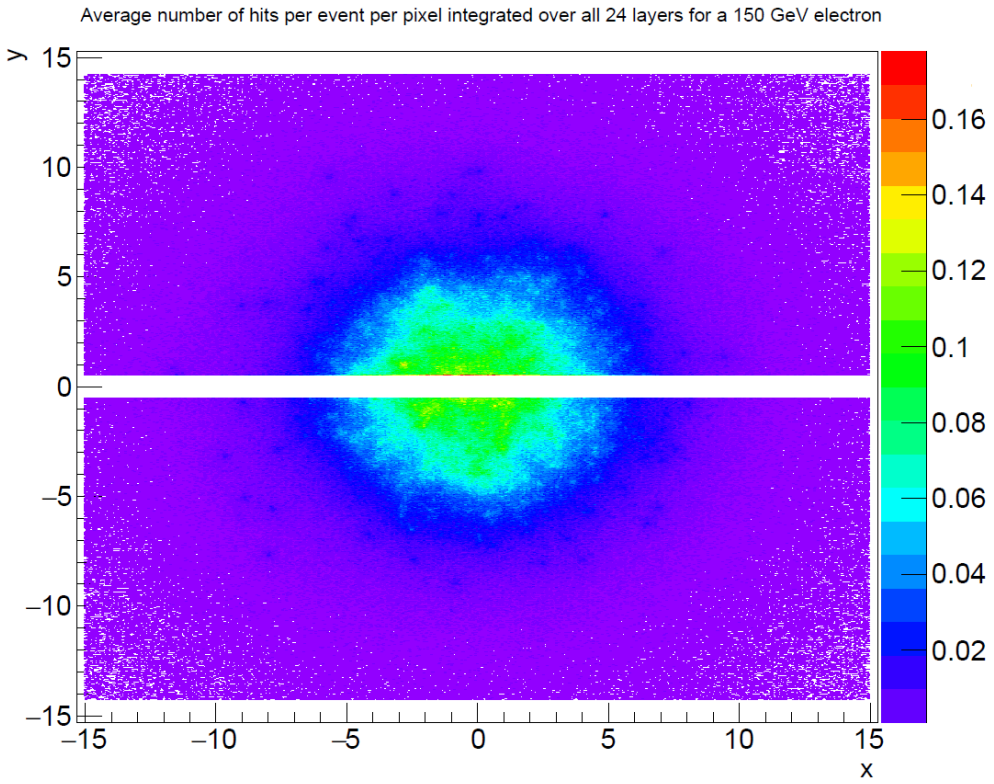

Figure 10: Average number of hits per event and per pixel area integrated over all layers as a function of the x and y position for 24 layers.

entered the detector there and created a shower. It can be seen in figure 8 that there is only a handful of particles that enter very far from the center. The average number of hits per event for the 24 layers also contains only a handful of clusters of increased activity, so this corresponds to those few particles that entered the detector very far from the center. The activity near the gap of the two chips, so at the 511th and 512th y pixel, seems to be slightly increased. This is most likely caused by erroneous double counting in the simulation or data analysis. An increase in the energy of the electron creates the same distribution but with a higher average number of hits per pixel.

The energy distribution for the energy deposited per active pixel is shown in figure 11 for two different energy ranges. The plot for the energy range 0 to 2000 keV shows that the majority of the pixels will have a low amount of energy deposited in them. There is a curious drop at 400 keV for which no explanation has been found. The plot for the energy range of 0 to 30 shows a clear peak in energy deposition at around 7 keV. Given the shape of this energy distribution it might be reasonable to use a threshold for the pixels to be active of 3 keV, which is right at the start of the peak activity. It is also interesting to note that the tail of the energy distribution is extremely long, as can also be seen from the plot on the left. While the number of entries with such energies is very low, it does have a serious contribution to the total energy deposited. For the larger energy range the average is 12.83 keV, which is significantly higher than the average energy for the smaller energy range of 8.935 keV. This

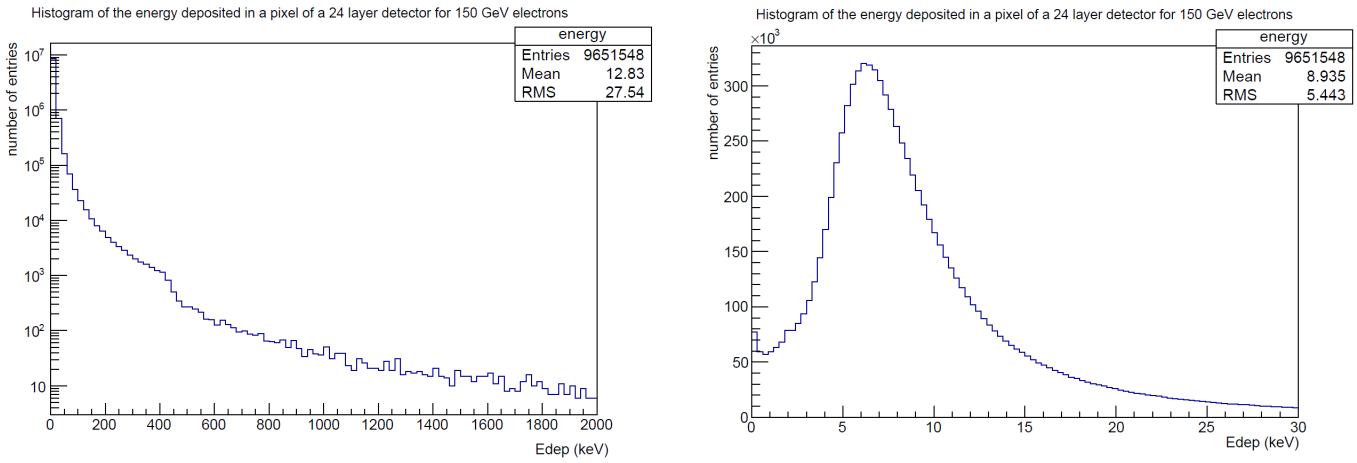

Figure 11: The energy distribution for a 24 layer detector for electrons of 150 GeV for two different energy ranges.

means that the tail contributes to more than 25% of the total energy that is deposited.

Figure 12 shows the distribution of the number of hits per event for electron energies of 50, 100, 150 and 180 GeV. The average number of hits for electrons of 50 GeV is 3338 with an RMS of 369.3. The average number of hits for electrons of 100 GeV is 6553 with an RMS of 713.6. The average number of hits for 150 GeV is 9652 with an RMS of 1053 and lastly the average number of hits for 180 GeV is 11490 with a RMS of 1238. The average amount of hits per event seems to increase linearly with the energy of the electron. The distribution contains a smaller peak followed by a larger peak. The spread between the peaks increases as the energy increases. The smaller peak is not present in the simulation for the ideal detector as can be seen from figure 9. The gap between the two chips could explain this smaller peak. If the electron enters the detector somewhere between the two chips, it will deposit most of its energy and cause most of the hits near the point of entry. This is also very clear in figure 7. However, there is no detector in the gap so most of this particle's shower is contained in an area that is not detected. The particle shower appears to barely be wide enough to still generate some particles far enough from the point of entry that there is still a reasonable number of hits. So it seems plausible that the smaller peaker represents particles that enter in the gap between the two chips and thus don't generate as many hits as they would if they hit the detector somewhere else. A fit has been made for the energy of the electron versus the average number of hits per event. The result is shown in figure 13. The number of hits per events increases linearly with the electron energy.

4.3 4 layers

The average hits per event per pixel area integrated over all layers as a function of the position in x and y is shown in figure 14 for a detector of 4 layers and an electron of 150 GeV. The distribution of hits is much less continuous than for the 24 layer detector. This is because the particle shower is still relatively limited for 4 layers. This means that the particle's energy is mostly distributed close to where the particle enters the detector. This makes the

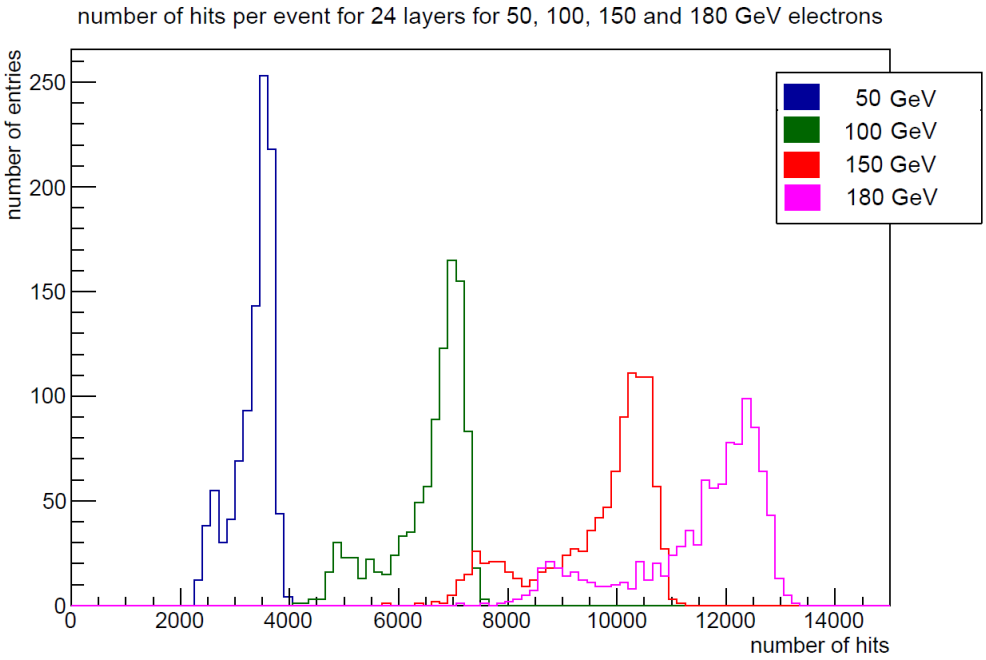

Figure 12: The distribution of the number of hits per event for a detector of 24 layers for 50, 100, 150 and 180 GeV electrons.

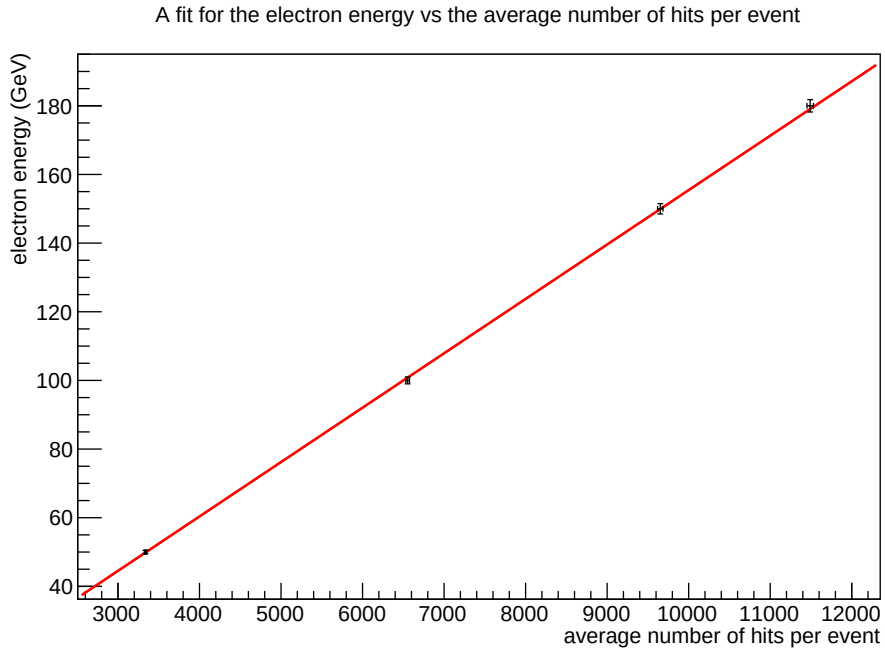

Figure 13: A fit of the energy of the electron versus the average number of hits per event for a 24 layer detector.

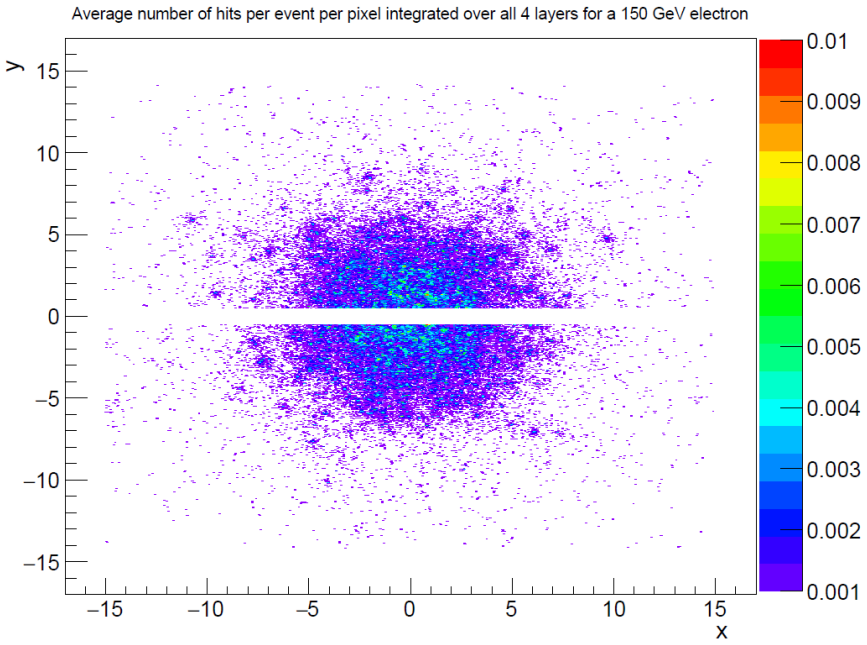

Figure 14: Average number of hits per event and per pixel area integrated over all layers as a function of of the x and y position for 4 layers.

hit distribution resemble the discrete spread of the particle source, which can be seen in figure 8, more. As the particles travel a larger distance through the absorber, they create more secondary particles and deposited their energy in a larger area. This means that the hit distribution should appear more continuous as the amount of layers of the detector increases.

Figure 15 shows the energy distribution of the deposited energy per pixel for a 150 GeV electron. The graph on the left shows that most of the active pixels have a low amount energy deposited in them. The amount of pixels with a high energy deposition is significantly lower than what is the case for a detector of 24 layers, as can be seen in figure 12. The graph on the right shows a similair peak energy deposition at around 7 keV. Once again the start of this peak is at about 3 keV, which reinforces the idea of implementing a threshold for a pixel to be active at 3 keV. The long tail of higher energy once more has a significant impact on the average energy per pixel. The average energy deposited in a pixel from an energy range of 0 to 30 keV is 8.534 keV, while the average energy deposited in a pixel for an energy range of 0 to 1500 keV is 11.88.

Figure 16 shows the distribution of the number of hits per event for electron energies of 50, 100, 150 and 180 GeV. The average amount of hits per event increases as the energy of the electron increases. However the relative increase is much smaller than the increase for a detector of 24 layers. The peaks are also overlapping much more compared to the peaks for 24 layers. For a detector of only 4 layers it is hard to observe a secondary peak similar to the secondary peak in figure 12 because the number of hits is much smaller and thus statistical deviations are more relevant. A fit has been made for the energy of the electron versus the

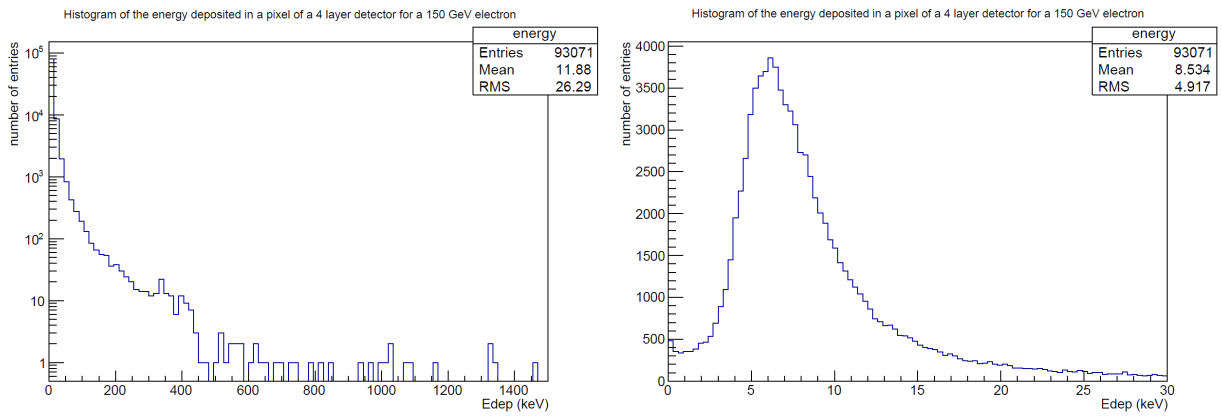

Figure 15: The energy distribution for a 4 layer detector for electrons of 150 GeV for two different energy ranges.

average number of hits per event. The result is shown in figure 17. The number of hits per events seems to increase linearly with the electron energy, although the results do not quite match this linear behaviour. This is probably due to statistical fluctuations, since the number of hits is very small for a 4 layer detector.

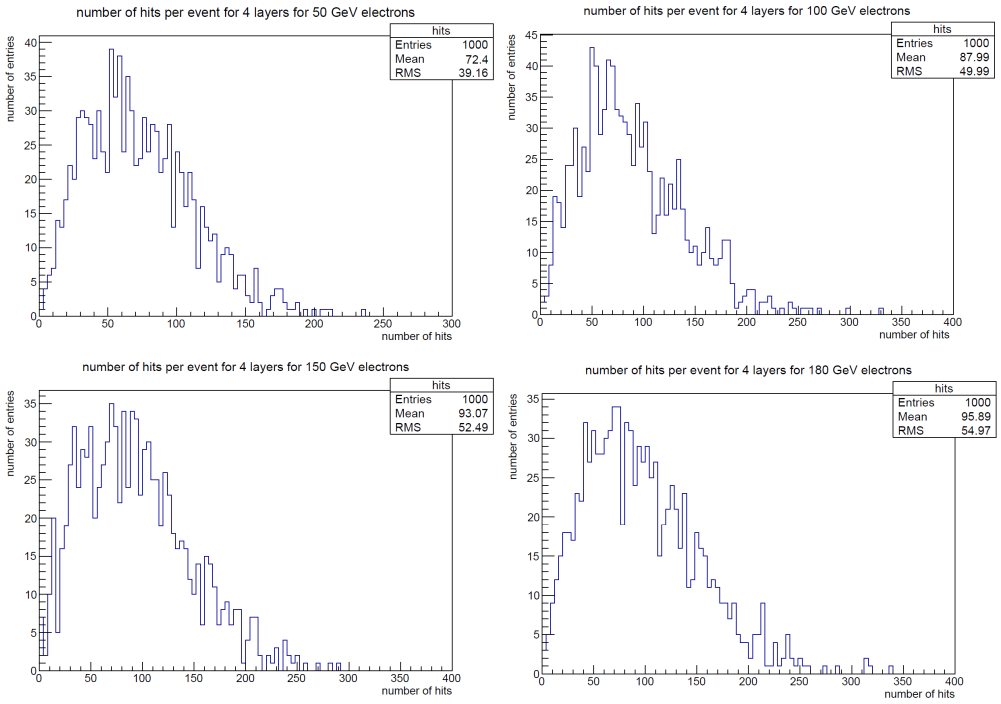

Figure 16: The distribution of the number of hits per event for a detector of 4 layers for 50, 100, 150 and 180 GeV electrons.

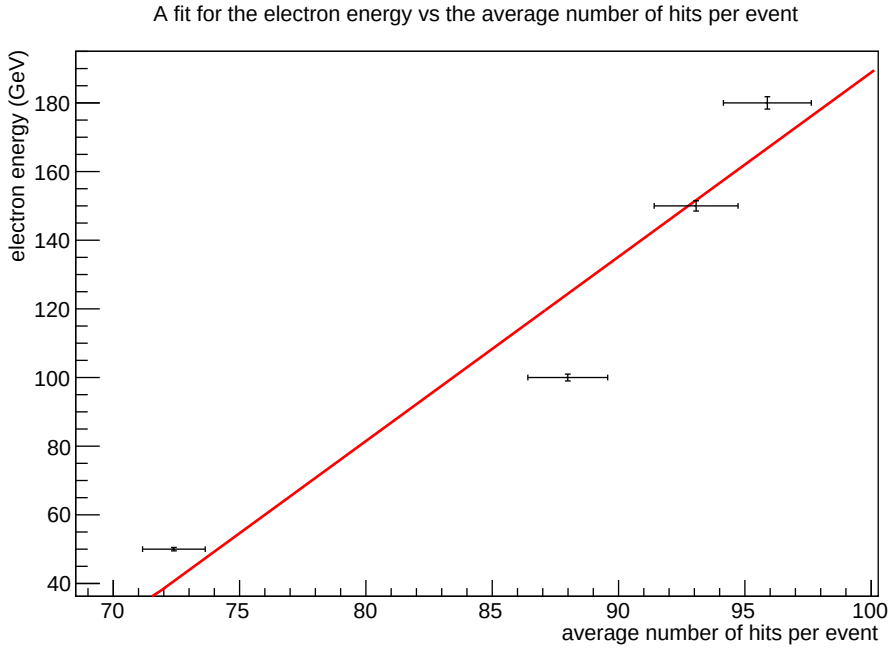

Figure 17: A fit of the energy of the electron versus the average number of hits per event for a 4 layer detector.

4.4 one layer

Figure 18 shows the average hits per event per pixel area integrated over all layers as a function of the position in x and y for a detector of 4 layers and an electron of 150 GeV for the one layer detector set up with no absorber and an absorber of 8, 20 and 28 mm tungsten in front of it. When there is no absorber in front of the detector we simply find the point at which the particle enters the detector. This is thus similar to the spread plotted in figure 8, as expected. In the case of an absorber that is 8 mm thick, we find a result that is similar to the result for the 4 layer detector but with less hits on average. This is because an absorber of 8 mm corresponds to a detector of about 2.5 layers. There are fewer secondary particles depositing energy than what is the case for the 4 layer detector. As the thickness of the absorber increases it reaches the maximum of the shower. We see that the average number of hits also increases as the thickness of the absorber increases to 20 and 28 mm. It can be seen from the benchmark simulation in figure 6 that the shower maximum occurs at the 11th layer. In this case the particle has traversed 10 layers of tungsten with a thickness of 3 mm each for a total of 30 mm. This means that the plot for a 28 mm tungsten absorber should be very close to the maximum of the shower.

The distribution of the number of hits per event for one layer with an 8 mm tungsten absorber in front of it is shown in figure 19. The average number of hits per event increases only very slightly as the energy of the particle increases and the overlap in the distributions is very large. Again, a fit has been made for the energy of the electron versus the average number of hits per event. The result is shown in figure 20. The number of hits per events seems to increase linearly with the electron energy, although as for the 4 layer simulation these results also do not quite match this linear behaviour.

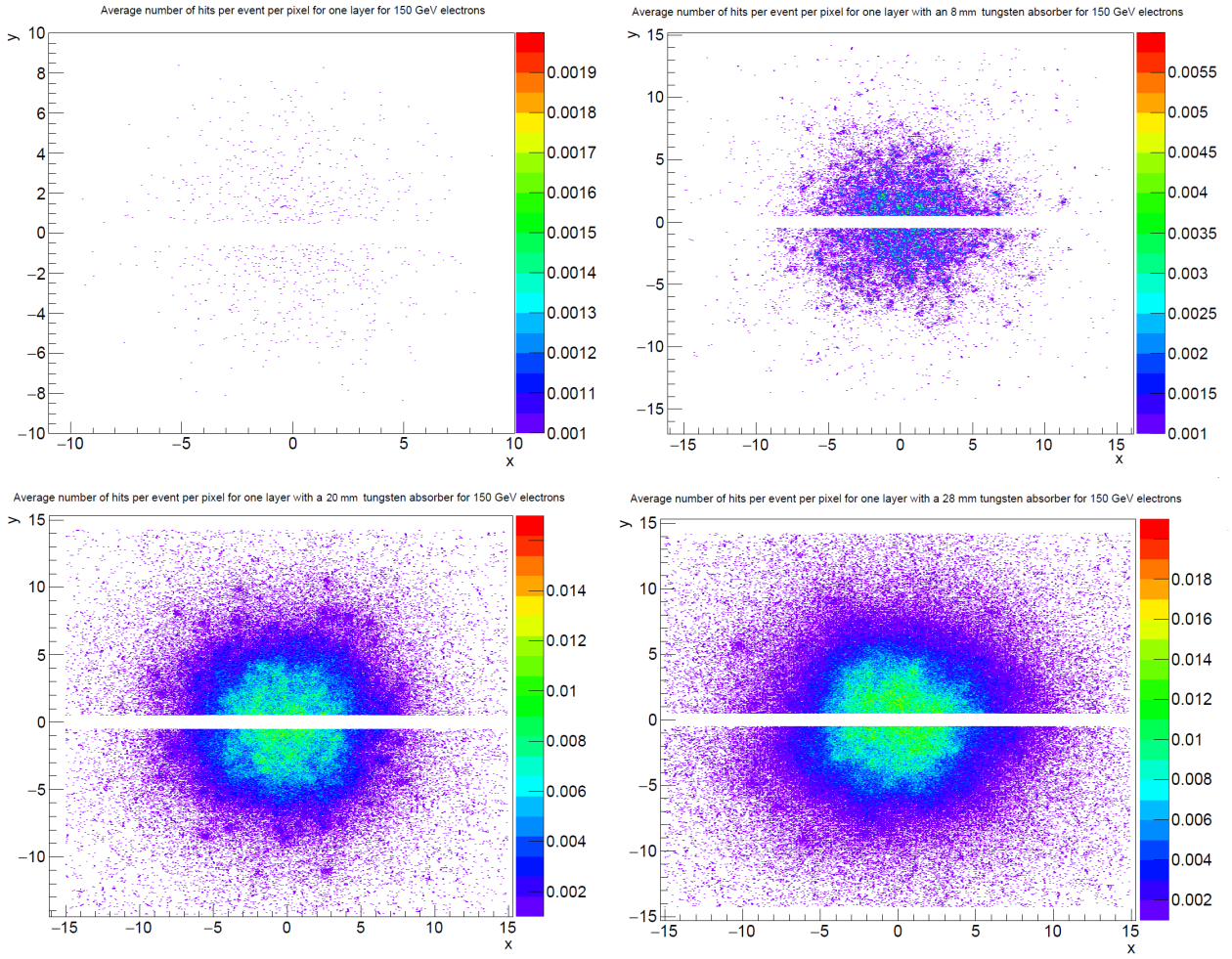

Figure 18: Average number of hits per event and per pixel area integrated over all layers as a function of pixel number in x- and y-direction for a one layer detector with no absorber and an absorber of 8, 20 and 28 mm tungsten in front of it for electrons of 150 GeV.

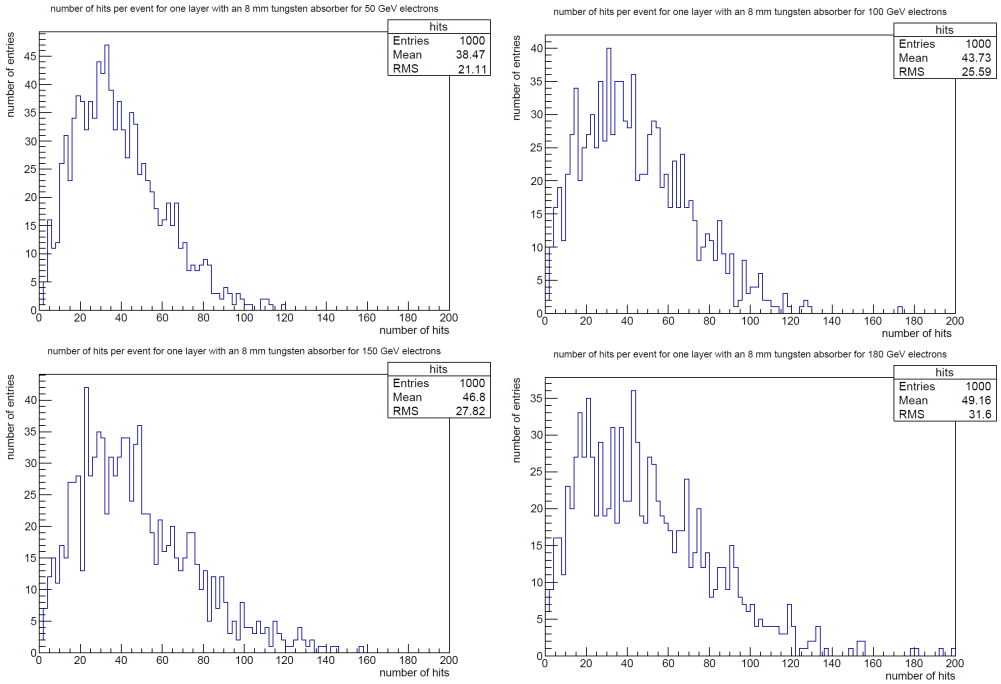

Figure 19: The distribution of the number of hits per event for a detector of one layer with an 8 mm tungsten absorber in front of it for 50, 100, 150 and 180 GeV electrons.

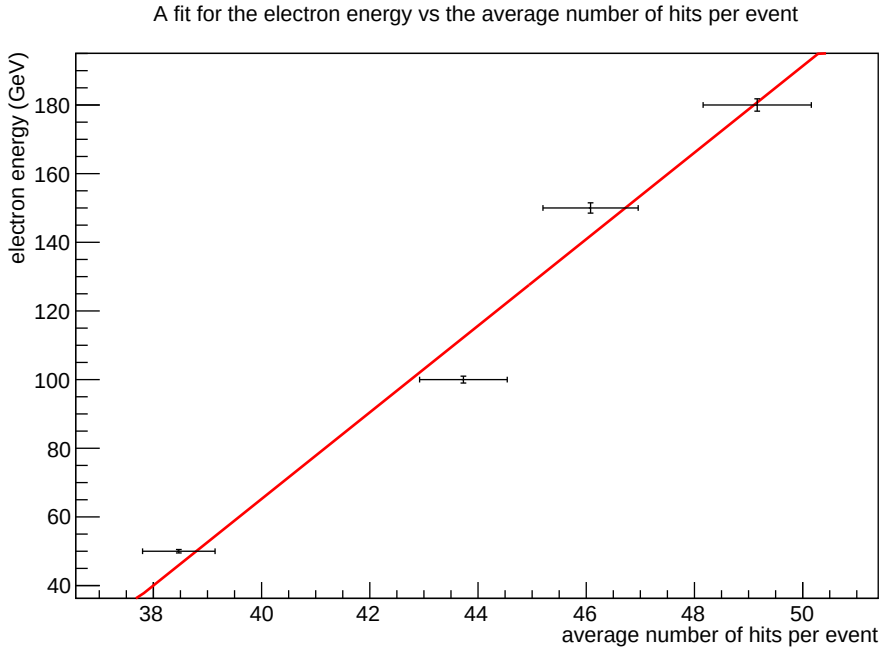

Figure 20: A fit of the energy of the electron versus the average number of hits per event for a detector of one layer with an 8 mm tungsten absorber in front of it.

5 Conclusion

The results show expected behaviour. The incoming particles create a shower inside the detector which can be measured by the ALPIDE CMOS sensors. The shower peak appears to be at about 11 radiation lengths. The energy per hit per pixel is distributed as expected. The vast majority of the energies of the hits is very small. The number of hits per event shows a secondary smaller peak for a smaller number of hits than the main peak for a 24 layer detector. This can be caused by the fact that the two seperate sensor chips are not placed exactly next to eachother. The smaller peak could then correspond to particles that hit the detector at the gap between the two chips. This hypothesis is backed up by the hits per event for a 24 layer detector without a gap between the chips, where this secondary peak is absent.

6 Discussion

In the simulation a handful of approximations have been made. These mostly have to do with the way the flex cable was simulated, for which the geometry was simplified a lot. It is possible to do new simulations where this geometry is defined more specifically, however the effect of this should be minimal as the flex is very thin compared to the rest of the detector.

It could be useful to look more closely at the secondary peak in the hit distribution for the 24 layer simulations. The explanation that the gap between the chips is responsible for this peak is backed up by the fact that this secondary peak disappears when the gap between the chips is removed. It would be interesting to do a simulation where the particles are directed at this gap and see if that produces only the secondary peak that we see in the graphs. This would confirm the theory that the gap is responsible for this peak.

Geant4's FTFP_BERT physics list was used for these simulations, which is one of the two recommended physics lists for this sort of simulation. It would be interesting to compare these results to simulations that use the other recommended physics list, QGSP_BERT.

In this simulation there was no threshold for the deposited energy required to activate a pixel. In reality there is a threshold before a pixel is active to filter out background noise. The graphs for the energy per hit per pixel imply that new simulations could be done with a threshold of 3 keV without losing many hits. However ideally the threshold used should match the threshold that is used in practice.

In practice not all pixels of the sensors work properly. Some of them are always on while some of then appear to not work at all. To do the data analysis these are taken out of the data.The comparison of experiments to this simulations could be made easier by including these dead pixels in the code of the simulation.

References

[1] W. Thompson, Popular lectures and addresses **1**, 73 (1883).

[2] *Lhc experiments*, URL https://home.cern/science/experiments.

[3] C. Pralavorio, *Time for lead collisions in the lhc* (2018), URL https://home.cern/news/news/accelerators/time-lead-collisions-lhc.

[4] *Alice*, URL https://home.cern/science/experiments/alice.

[5] *Alice physics*, URL http://aliceinfo.cern.ch/Public/en/Chapter1/Chap1Physics-en.html.

[6] *Detectors of the alice experiment*, URL http://aliceinfo.cern.ch/Public/en/Chapter2/Page3-subdetectors-en.html.

[7] *Upgrade of the alice experiment: Letter of intent* (2012), URL http://cds.cern.ch/record/1475243.

[8] T. Peitzmann, *Prototype studies for a forward em calorimeter in alice* (2013), URL https://arxiv.org/abs/1308.2585.

[9] C. W. Fabjan and F. Gianotti, Review of Modern Physics **75** (2003).

[10] C. Grupen and B. Shwartz, *Particle Detectors* (Cambridge University Press, 2008), 2nd ed., ISBN 978-0-511-38866-8.

[11] *Atomic and nuclear properties of materials for more than 300 materials* (2018), URL http://pdg.lbl.gov/2018/AtomicNuclearProperties/.

[12] S. Borshchov, I. Tymchuck, M. Protsenko, Y. Taranova, T. Peitzmann, and T. van den Brink, *Technological mock-up of detector layer for focal mtower* (2017), URL https://indico.cern.ch/event/679708/contributions/2791139/attachments/1558631/2452680/FoCal_meeting_at_CERN_-LTU-NIKHEF_2017_11_15-7-F-2.pdf.

[13] Geant4-Collaboration, *Physics reference manual*, URL http://geant4-userdoc.web.cern.ch/geant4-userdoc/UsersGuides/PhysicsReferenceManual/html/index.html.

[14] N. Srimanobhas, *Introduction to monte carlo for particle physics study*.

[15] *The monte carlo method*, URL http://www2.pv.infn.it/~fontana/download/lect/cadi7.pdf.

[16] M. A. Cortés-Giraldo, *Short guide to choosing a physics list*.

[17] D. Wright and S. Incerti, *A short guide to choosing physics lists*.

[18] Geant4-Collaboration, *Use cases - reference physics lists*, URL https://geant4.web.cern.ch/node/302l.

A Appendix

The figures for the electrons of 50, 100 and 180 GeV are shown here.

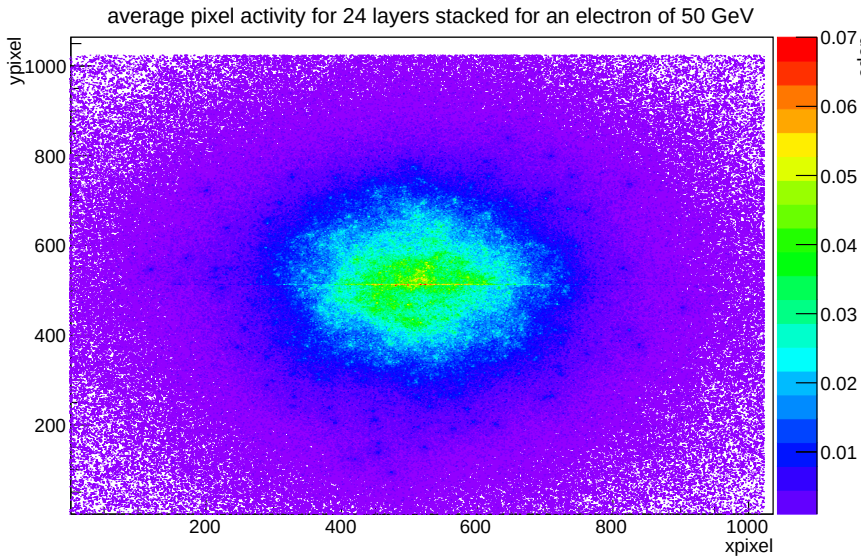

Figure 21: Average number of hits per event and per pixel area integrated over all layers as a function of pixel number in x- and y-direction for 24 layers for an electron of 50 GeV.

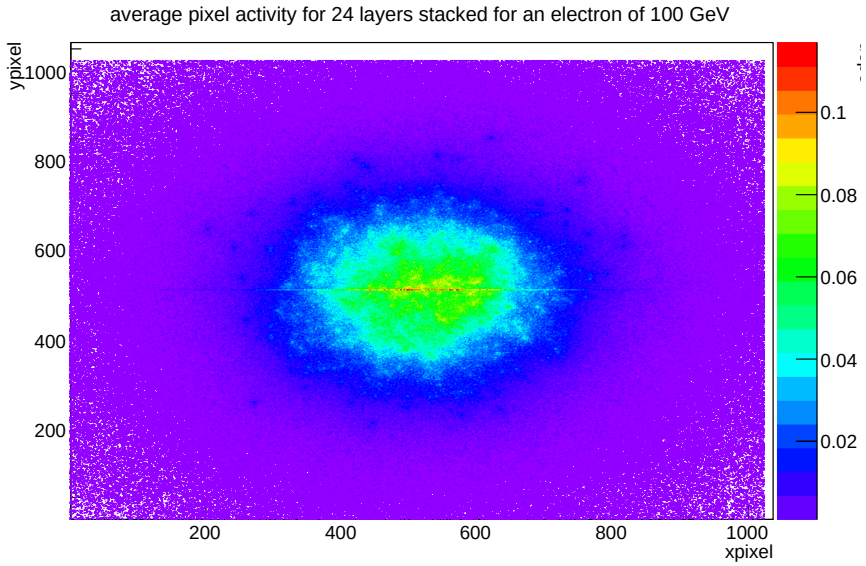

Figure 22: Average number of hits per event and per pixel area integrated over all layers as a function of pixel number in x- and y-direction for 24 layers for an electron of 100 GeV.

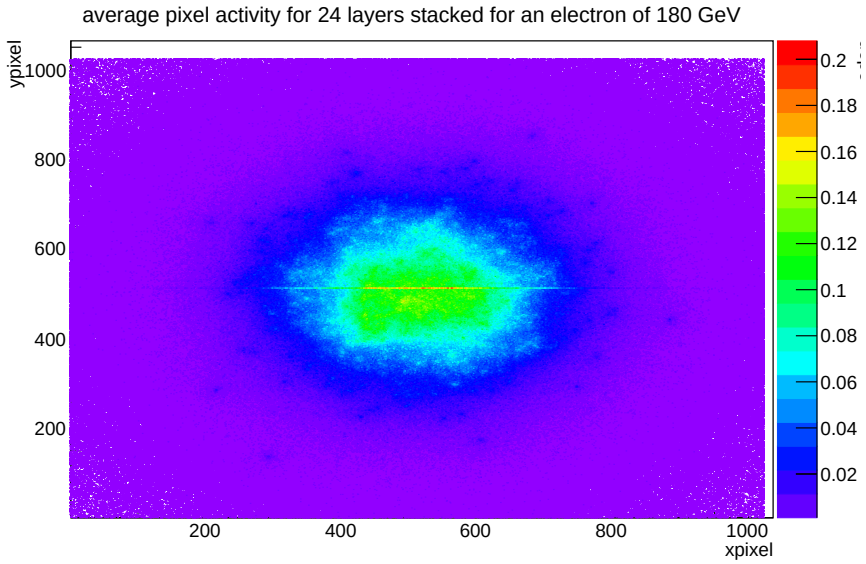

Figure 23: Average number of hits per event and per pixel area integrated over all layers as a function of pixel number in x- and y-direction for 24 layers for an electron of 150 GeV.

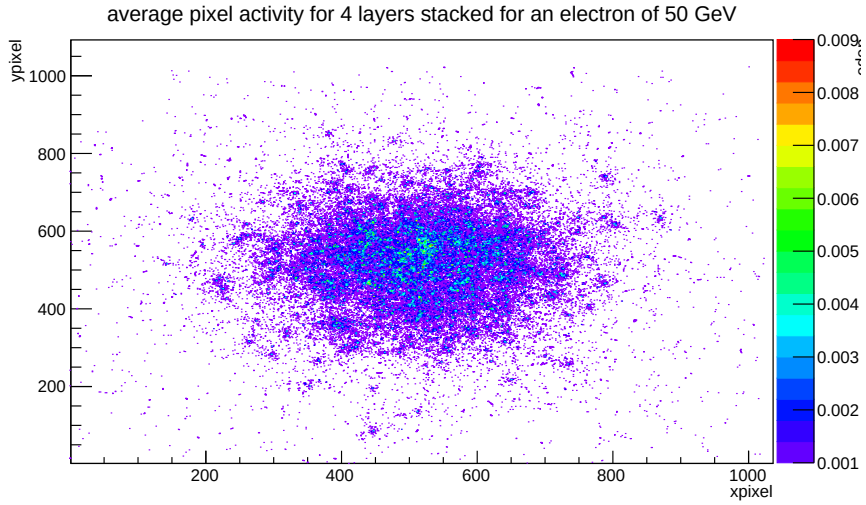

Figure 24: Average number of hits per event and per pixel area integrated over all layers as a function of pixel number in x- and y-direction for 4 layers for an electron of 50 GeV.

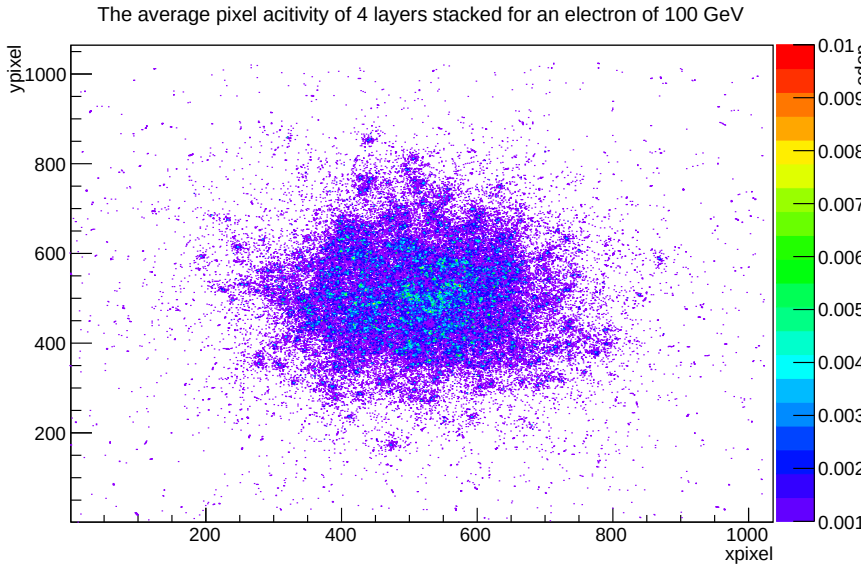

Figure 25: Average number of hits per event and per pixel area integrated over all layers as a function of pixel number in x- and y-direction for 4 layers for an electron of 100 GeV.

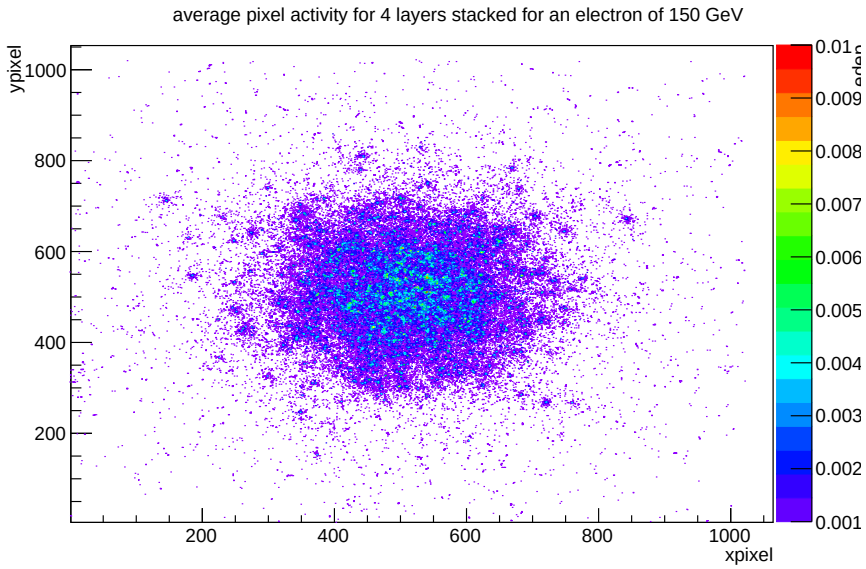

Figure 26: Average number of hits per event and per pixel area integrated over all layers as a function of pixel number in x- and y-direction for 4 layers for an electron of 180 GeV.

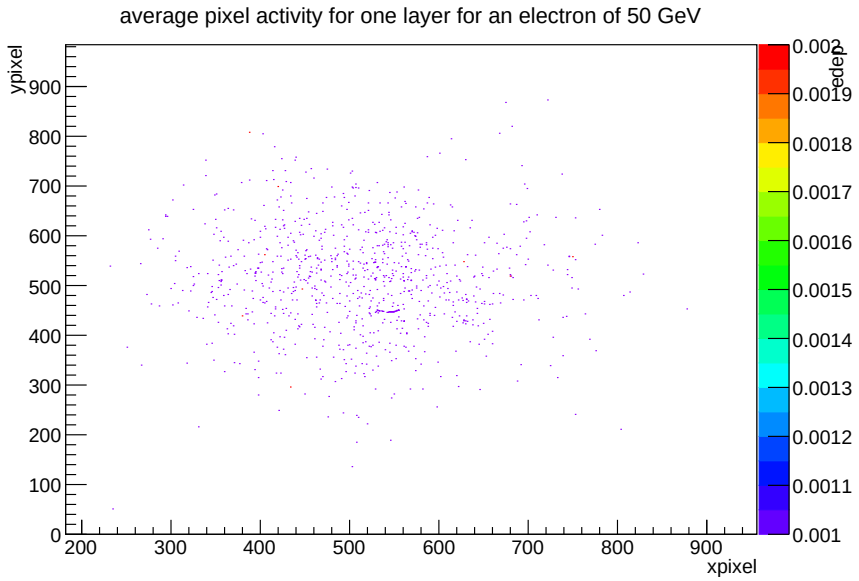

Figure 27: Average number of hits per event and per pixel area as a function of pixel number in x- and y-direction for one layer for an electron of 50 GeV.

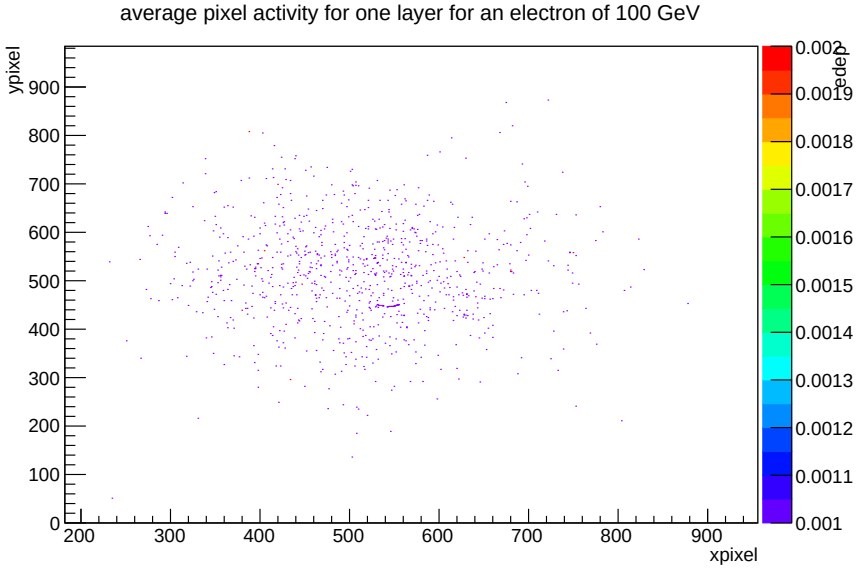

Figure 28: Average number of hits per event and per pixel as a function of pixel number in x- and y-direction for one layer for an electron of 100 GeV.

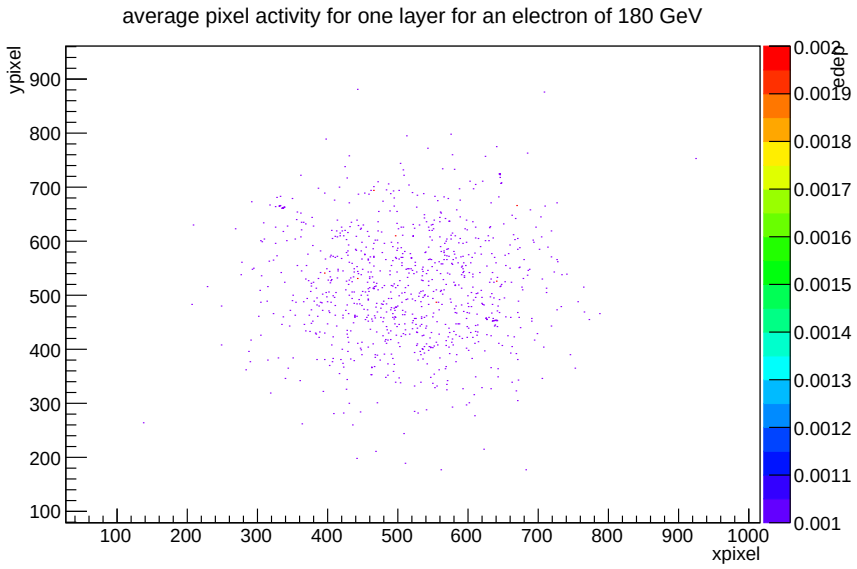

Figure 29: Average number of hits per event and per pixel as a function of pixel number in x- and y-direction for one layer for an electron of 180 GeV.

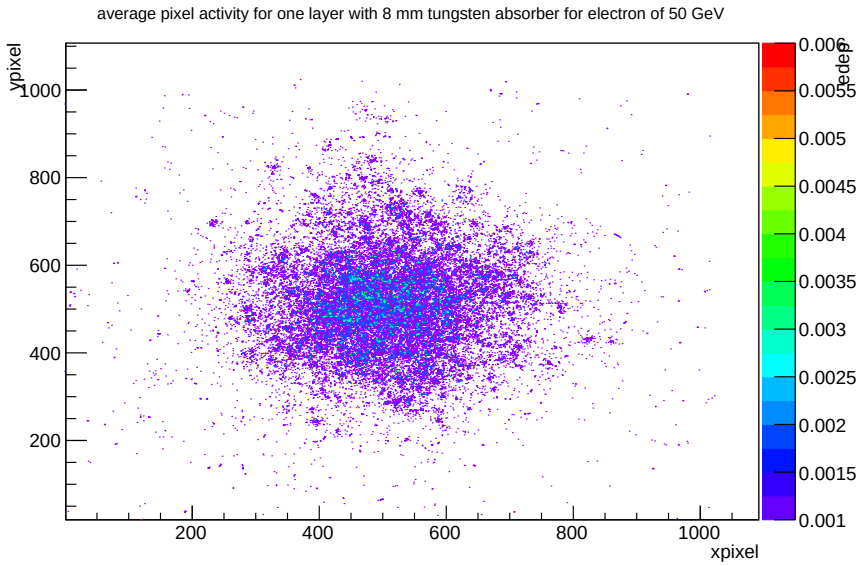

Figure 30: Average number of hits per event and per pixel area as a function of pixel number in x- and y-direction for one layer with an 8 mm absorber in front of it for an electron of 50 GeV.

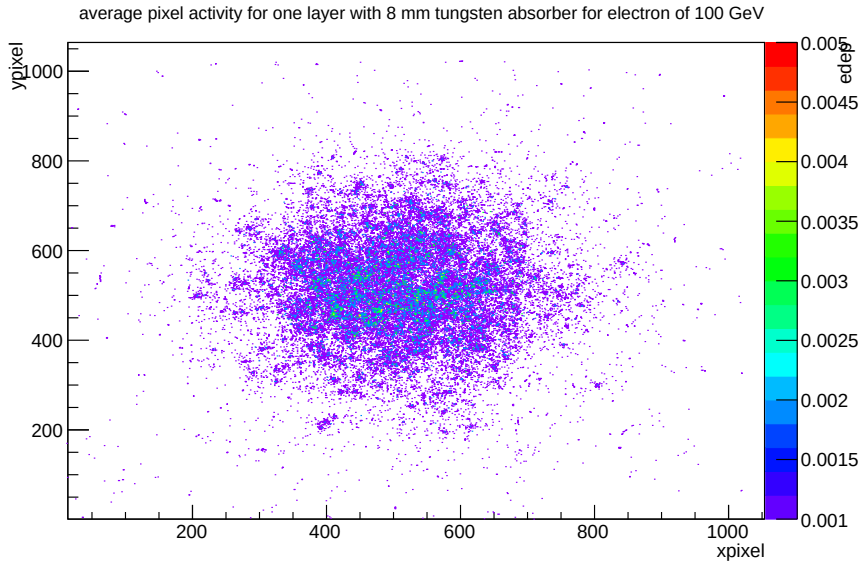

Figure 31: Average number of hits per event and per pixel as a function of pixel number in x- and y-direction for one layer with an 8 mm absorber in front of it for an electron of 100 GeV.

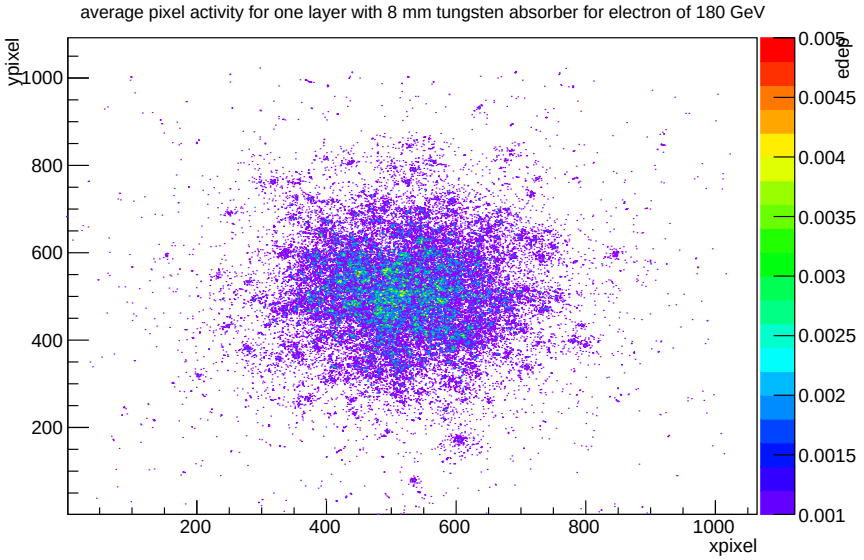

Figure 32: Average number of hits per event and per pixel as a function of pixel number in x- and y-direction for one layer with an 8 mm absorber in front of it for an electron of 180 GeV.

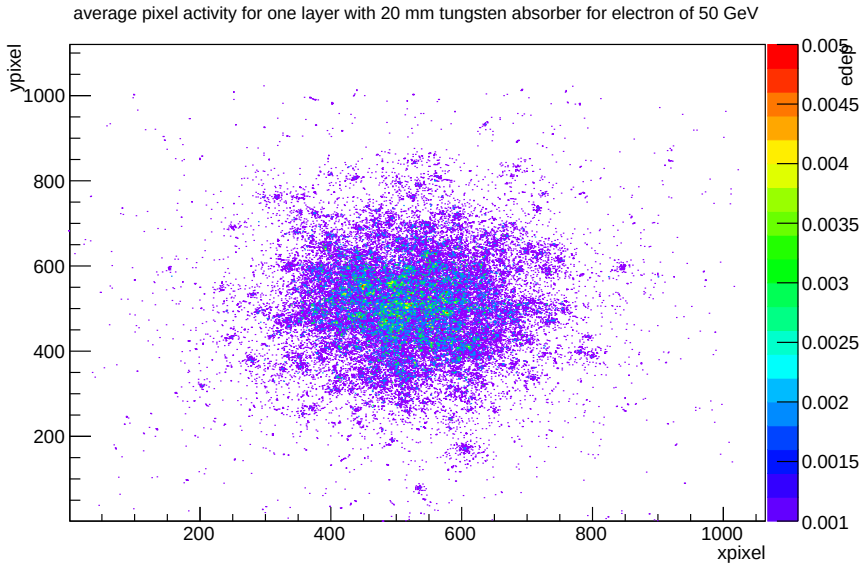

Figure 33: Average number of hits per event and per pixel area as a function of pixel number in x- and y-direction for one layer with an 20 mm absorber in front of it for an electron of 50 GeV.

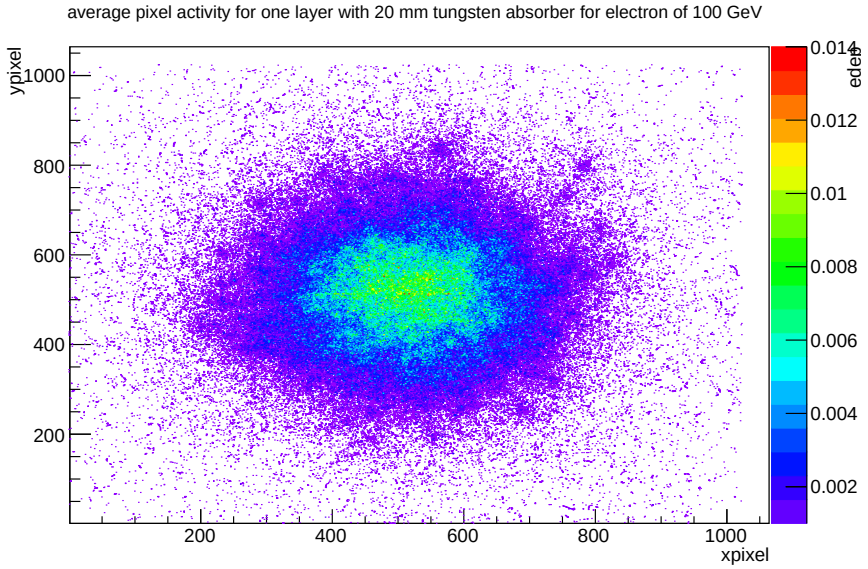

Figure 34: Average number of hits per event and per pixel as a function of pixel number in x- and y-direction for one layer with an 20 mm absorber in front of it for an electron of 100 GeV.

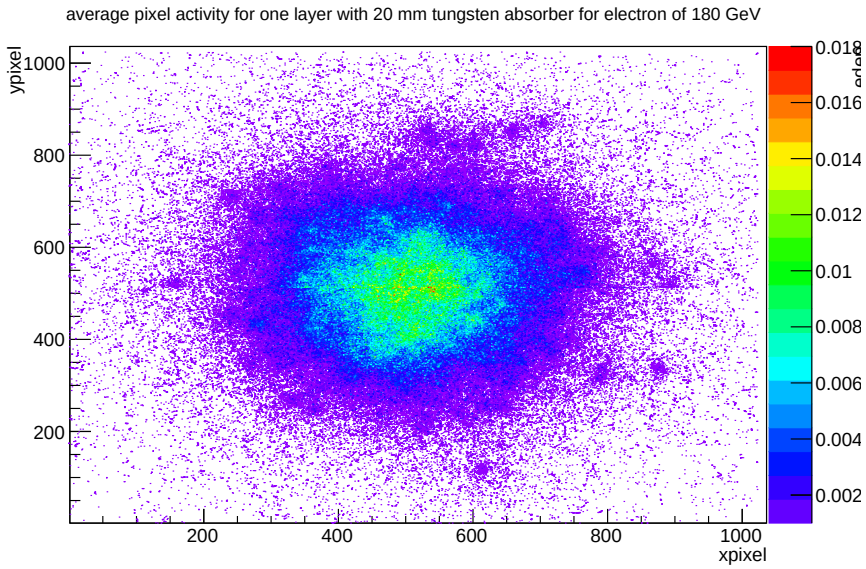

Figure 35: Average number of hits per event and per pixel as a function of pixel number in x- and y-direction for one layer with an 20 mm absorber in front of it for an electron of 180 GeV.

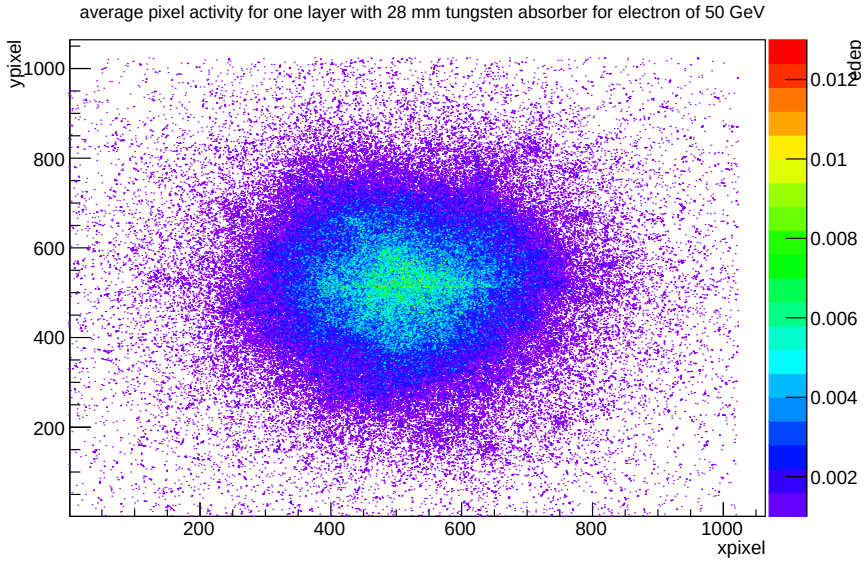

Figure 36: Average number of hits per event and per pixel area as a function of pixel number in x- and y-direction for one layer with an 28 mm absorber in front of it for an electron of 50 GeV.

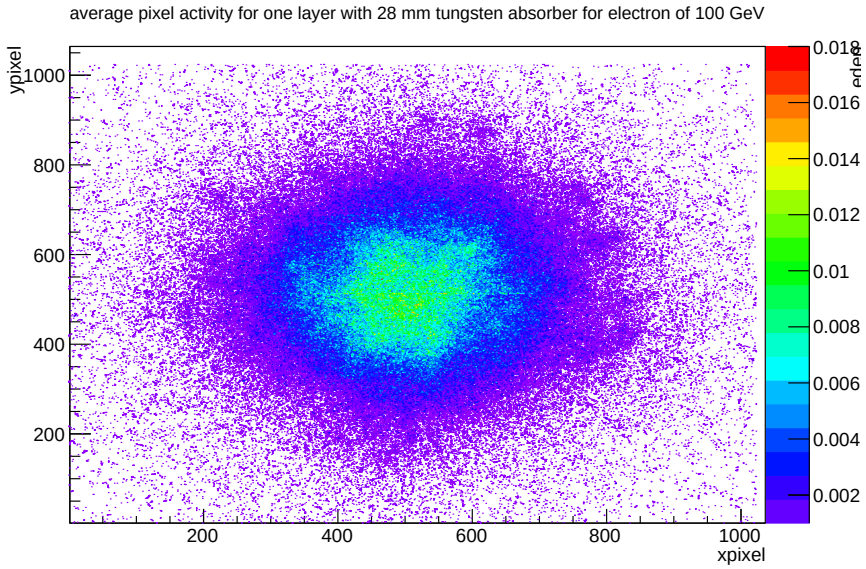

Figure 37: Average number of hits per event and per pixel as a function of pixel number in x- and y-direction for one layer with an 28 mm absorber in front of it for an electron of 100 GeV.

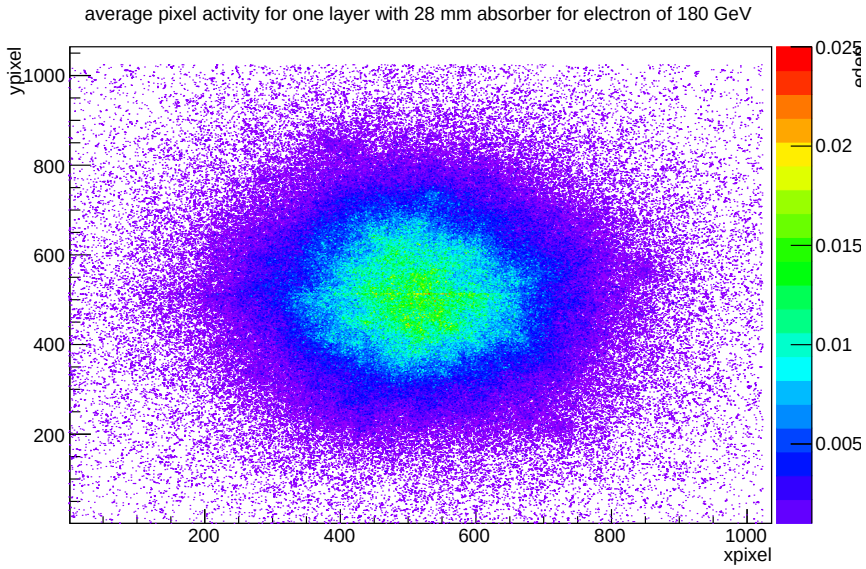

Figure 38: Average number of hits per event and per pixel as a function of pixel number in x- and y-direction for one layer with an 28 mm absorber in front of it for an electron of 180 GeV.